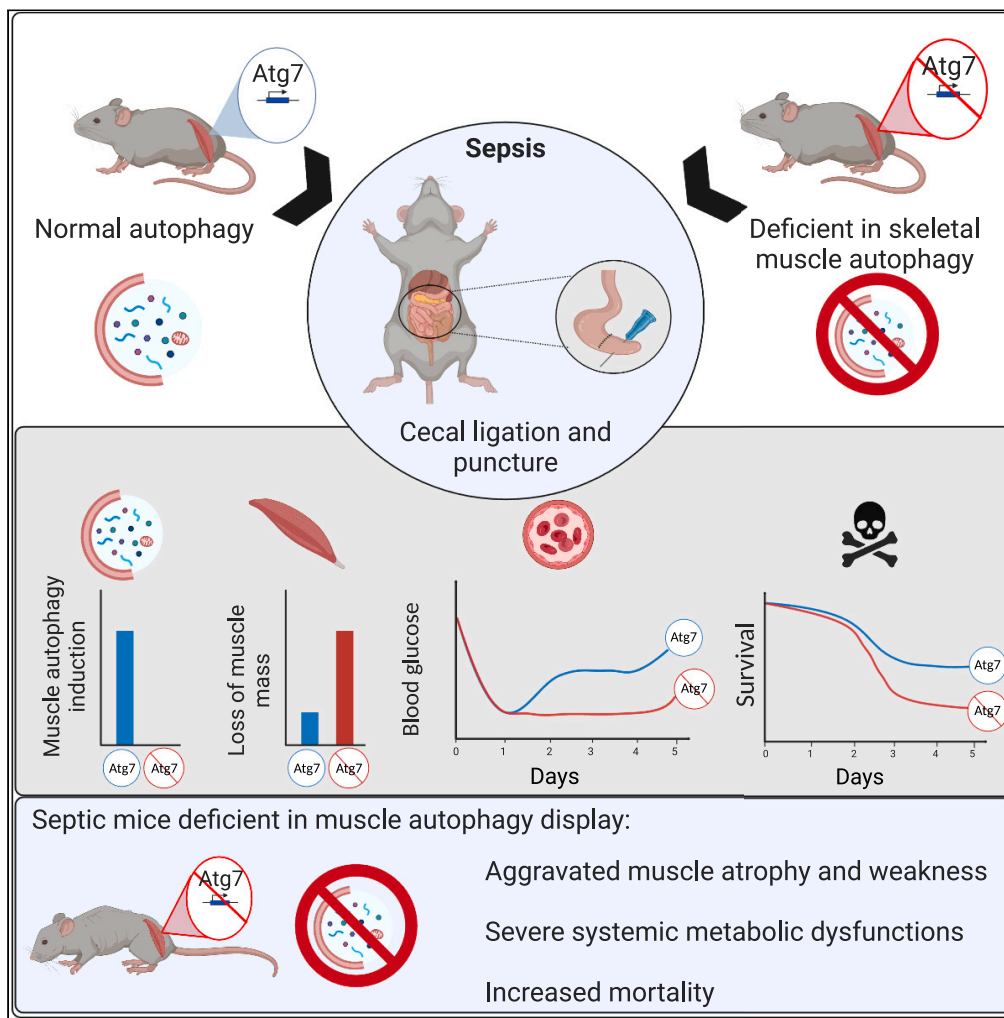# iScience

Article

Autophagy ablation in skeletal muscles worsens sepsis-induced muscle wasting, impairs whole-body metabolism, and decreases survival

Jean-Philippe
Leduc-Gaudet,
Kayla Miguez,
Marina Cefis, ...,
Marco Sandri,
Gilles Gouspillou,
Sabah N.A.
Hussain

jean-philippe.leduc.gaudet@
uqtr.ca (J.-P.L.-G.)
gouspillou.gilles@uqam.ca
(G.G.)
sabah.hussain@muhc.mcgill.
ca (S.N.A.H.)

Highlights

Sepsis-induced muscle
wasting is associated with
an activation of autophagy

Autophagy inactivation in
skeletal muscles worsens
muscle wasting during
sepsis

Septic autophagy
deficient mice display
metabolic alterations and
reduced survival

Autophagy activation in
muscles during sepsis is
protective and pro-
survival

iScience

Article

Autophagy ablation in skeletal muscles worsens sepsis-induced muscle wasting, impairs whole-body metabolism, and decreases survival

Jean-Philippe Leduc-Gaudet,[1,2,3,4,*] Kayla Miguez,[2,3] Marina Cefis,[3,4] Julie Faitg,[4,5] Alaa Moamer,[3] Tomer Jordi Chaffer,[2,3] Olivier Reynaud,[4] Felipe E. Broering,[2,3] Anwar Shams,[6] Dominique Mayaki,[2,3] Laurent Huck,[2,3] Marco Sandri,[3,7] Gilles Gouspillou,[3,4,8,*] and Sabah N.A. Hussain[2,3,8,*]

SUMMARY

Septic patients frequently develop skeletal muscle wasting and weakness, resulting in severe clinical consequences and adverse outcomes. Sepsis triggers sustained induction of autophagy, a key cellular degradative pathway, in skeletal muscles. However, the impact of enhanced autophagy on sepsis-induced muscle dysfunction remains unclear. Using an inducible and muscle-specific *Atg7* knockout mouse model (Atg7[iSkM−KO]), we investigated the functional importance of skeletal muscle autophagy in sepsis using the cecal ligation and puncture model. Atg7[iSkM−KO] mice exhibited a more severe phenotype in response to sepsis, marked by severe muscle wasting, hypoglycemia, higher ketone levels, and a decreased in survival as compared to mice with intact *Atg7*. Sepsis and *Atg7* deletion resulted in the accumulation of mitochondrial dysfunction, although sepsis did not further worsen mitochondrial dysfunction in Atg7[iSkM−KO] mice. Overall, our study demonstrates that autophagy inactivation in skeletal muscles triggers significant worsening of sepsis-induced muscle and metabolic dysfunctions and negatively impacts survival.

INTRODUCTION

Sepsis is a leading cause of death in intensive care units. Several prospective and retrospective studies have confirmed that ventilatory and limb muscle dysfunction occurs in most septic patients.[1,2] Ventilatory muscle dysfunction leads to difficult weaning of patients from mechanical ventilation and recurrence of respiratory failure after weaning.[3,4] Long-term ramifications of limb muscle dysfunction include functional limitations and poor quality of life.[5] Sepsis-induced multiple organ failure and muscle inactivity are among the risk factors for development of severe muscle dysfunction. Primary manifestations include impaired contractility and atrophy of muscle fibers.

Sepsis-induced muscle atrophy has been primarily attributed to increased protein degradation. Indeed, it has been shown in muscles of septic rats that total and myofibrillar protein degradation increases by 50% and 440%, respectively,[6] and that myofibrillar protein breakdown by the ubiquitin system is enhanced. Proteolysis in skeletal muscles is regulated by four pathways: the calpain, caspase-3, ubiquitin-proteasome, and autophagy pathways. The first three are responsible for degradation of myofilament proteins. Calpains and caspase-3 are strongly activated in limb and ventilatory muscle fibers during sepsis.[7–9] Several components of the ubiquitin-proteasome system, including the muscle-specific ubiquitin E3 ligases *Fbxo32* (Atrogin-1) and *Trim63* (MuRF1) and 20S subunits, are upregulated in the ventilatory and limb muscles in animal models of sepsis,[10–13] and activation of the ubiquitin-proteasome system is believed to play an important role in sepsis-induced muscle atrophy.[14–16]

Autophagy is a complex process primarily responsible for the degradation of cytoplasmic proteins and organelles, including mitochondria and peroxisomes. Three main types of autophagy have been documented: microautophagy, chaperone-mediated autophagy, and macroautophagy.[17] Among them, macroautophagy (hereafter referred to as autophagy) has been the most extensively studied in skeletal muscles and it was also shown that the contribution of autophagy to total muscle protein degradation

Figure 1. Muscle-specific deletion of Atg7 inhibits basal autophagy in skeletal muscles

(A) mRNA expressions of Atg7 in TA muscles of female Atg7$^{f/f}$ and Atg7$^{iSkM-KO}$ mice 48 h after sham surgery. Data presented as fold change relative to sham Atg7$^{f/f}$ mice.

(B) Representative immunoblots of Atg7, p62/SQSTM1, and LC3B proteins. GAS = gastrocnemius, PL = plantaris, SOL = soleus, TA = tibialis anterior.

(C and D) Immunostaining and quantification of the proportion of p62/SQSTM1 positive fibers in TA muscles of female Atg7$^{f/f}$ and Atg7$^{iSkM-KO}$ mice 48 h after sham surgery. Scale bars = 20μm.

(E) mRNA expressions of Atg7 in TA muscles of female Atg7$^{f/f}$ and Atg7$^{iSkM-KO}$ mice 48 h after CLP. 18S levels used as a control.

(F) Representative immunoblots of ATG7, p62/SQSTM1, and LC3B proteins in TA muscles of female Atg7$^{f/f}$ and Atg7$^{iSkM-KO}$ mice 48 h after sham surgery or CLP.

Figure 1. Continued

(G–I) Densitometric analyses of ATG7, p62/SQSTM1, and LC3B protein levels in TA muscles of female Atg7$^{f/f}$ and Atg7$^{iSkM-KO}$ mice 48 h after sham surgery or CLP.

(J and K) Immunostaining for p62/SQSTM1 in TA muscles of female Atg7$^{f/f}$ and Atg7$^{iSkM-KO}$ mice 48 h after CLP surgery. Scale bars = 20 μm, inset scale bar = 10 μm.

(L and M) mRNA expressions of various autophagy-related genes (M) and lysosomal cathepsin in TA muscles of female Atg7$^{f/f}$ and Atg7$^{iSkM-KO}$ mice 48 h after sham surgery or CLP. Gaba refers to Gabarapl1 and Becn1 refers to Beclin1. N = 6–8 group. Data in panels A, D, E, G, H, I, K, L, and M are presented as mean ± SEM. Number of animals indicated within bars, where applicable. *p < 0.05 vs. sham Atg7$^{f/f}$; #p < 0.05 for sepsis effect (i.e., sham Atg7$^{f/f}$ vs. CLP Atg7$^{f/f}$ or sham Atg7$^{iSkM-KO}$ vs. CLP Atg7$^{iSkM-KO}$); †p < 0.05 for sepsis plus knockout effect (i.e., CLP Atg7$^{f/f}$ vs. CLP Atg7$^{iSkM-KO}$).

can be just as high as that from the proteasome pathway.[18] Several groups have reported that autophagy is induced in skeletal muscles of mice and rats injected with bacterial lipopolysaccharide (LPS) and that its induction coincides with significant mitochondrial dysfunction, depressed muscle contractility, and the development of fiber atrophy.[19–22] In recent studies, we demonstrated that cecal ligation and puncture (CLP)-induced sepsis triggers prolonged activation of autophagy and fiber atrophy in limb muscles.[13,23] However, whether autophagy induction during sepsis is beneficial or detrimental remains unknown. Indeed, autophagy induction was shown to contribute to muscle atrophy caused by denervation and fasting.[18,24] Blocking autophagy was also shown to protect against ventilator induced diaphragmatic disease.[25] However, several studies have demonstrated that autophagy is a critical regulator of protein homeostasis and muscle mass and that its activation is required to prevent the accumulation of dysfunctional organelles and unwanted protein aggregate that would lead to muscle atrophy and dysfunction.[26,27]

To address functional roles of autophagy in sepsis-induced skeletal muscle dysfunction, we generated conditional muscle-specific knockout of the autophagy related 7 (Atg7) gene in mice. Our main hypotheses were that augmented autophagy serves as a protective mechanism designed to increase the recycling of dysfunctional organelles and protein aggregates inside septic muscles and that inactivation of autophagy exacerbates muscle loss during sepsis.

RESULTS

Sepsis-induced activation of autophagy in skeletal muscles is blocked by *Atg7* deletion

The physiological function of autophagy in septic skeletal muscles was investigated by crossing *Atg7*-floxed mice (*Atg7$^{f/f}$*) with a transgenic line of mice in which Cre-ER^{T2} is expressed under the control of a tamoxifen-inducible human skeletal actin (*HSA*) promoter. The muscle-specific *Atg7* knockout mice generated from this cross are hereafter referred to as Atg7$^{iSkM-KO}$ (Figure S1). Immunoblotting and PCR analyses showed that 48 h after undergoing a sham surgical operation, *Atg7* mRNA and ATG7 protein levels were markedly lower in the limb muscles of Atg7$^{iSkM-KO}$ mice relative to Atg7$^{f/f}$ mice, thereby confirming the efficacy of *Atg7* deletion (Figures 1A and 1B). Lower LC3B (lipidated form of LC3B) protein levels and higher p62/SQSTM1 protein levels (autophagosome substrate) indicate that autophagosome formation was also inhibited, further confirming that *Atg7* deletion exerts an inhibitory effect on basal autophagy (Figures 1A, 1C, 1D, and S2A–S2C). Heart ATG7 protein levels were unaffected, indicating that autophagy inactivation in this model is specific to skeletal muscles (Figure S2D). Any remaining traces of Atg7 (protein or mRNA) in the limb muscles might have come from endothelial cells, fibroblasts, macrophages, or blood cells, as *Atg7* is normally expressed in these cells.

We have previously reported that autophagy increases in the limb muscles of mice 48 h after sepsis is induced by CLP.[13,28] In line with our previous observations, we found that sepsis resulted in a significant increase in LC3BII levels and LC3B-II/LC3B-I ratio in various skeletal muscles (Figures 3A–3D). To confirm that autophagy was induced upon sepsis, the autophagic flux was assessed using a leupeptin-based assay[29] (Figure 3E). In septic animals, leupeptin treatment resulted in a further increase in the LC3B-II/I ratio (Figure 3F), indicating that autophagy flux increases in skeletal muscles upon sepsis induction.

To assess the functional importance of skeletal muscle autophagy in sepsis, sham operated and CLP-operated Atg7$^{f/f}$ and Atg7$^{iSkM-KO}$ mice were compared. Under septic conditions, *Atg7* mRNA expression, ATG7 protein level and LC3B-II/LC3B-I protein ratio was significantly lower in the limb muscles of Atg7$^{iSkM-KO}$ mice as compared to Atg7$^{f/f}$ mice (Figures 1E–1I). The higher levels of p62/SQSTM1 and LC3-I associated with the lower LC3B-II protein levels in muscles of Atg7$^{iSkM-KO}$ mice suggests that autophagosome formation is blocked in this mouse model in response to sepsis (Figures 1F–1I). Importantly, p62/SQSTM1 protein

accumulated in muscles of Atg7$^{iSkM-KO}$ mice but not in those of Atg7$^{f/f}$ mice (Figures 1J and 1K), providing further evidence of selective inactivation of autophagy via deletion of *Atg7*.

Further confirming that autophagy is induced in the tibialis anterior (TA) and gastrocnemius (GAS) muscles of Atg7$^{f/f}$ mice 48 h after CLP, protein levels of LC3BII, LC3B-II/LC3B-I ratio, and Bnip3, as well as mRNA expression of several autophagy-related genes (*Lc3b*, *Sqstm1*, *Bnip3*, *Bnip3L*), and the lysosomal gene *Ctsl* were all increased (Figures 1F–1M and S4A–S4F). Expressions of two autophagy-related genes, *Gabarapl1* and *Park2*, were differentially regulated, depending on the muscle; in the TA, *Gabarapl1* expression increased while *Park2* did not change (Figure 1L), whereas in the GAS, *Park2* increased while *Gabarapl1* did not change (Figure S4E). LC3B-II/LC3B-I ratio did not increase in the limb muscles of Atg7$^{iSkM-KO}$ mice in response to sepsis, but p62/SQSTM1 protein level did (Figures 1F–1I, S4C, and S4D). In response to sepsis, p62/SQSTM1 protein aggregates were observed in limb muscles of Atg7$^{iSkM-KO}$ mice (Figures 1J and 1K), suggesting that it accumulates because of autophagy inhibition. Interestingly, in response to sepsis, autophagy-related gene expressions in the TA and GAS muscles of Atg7$^{f/f}$ and Atg7$^{iSkM-KO}$ mice increased to a similar extent (Figures 1L, 1M, S2E, and S2F), suggesting that deletion of *Atg7* does not interfere with the transcriptional upregulation of these genes that occurs in severe sepsis. Taken altogether, these data indicate that autophagy is induced in skeletal muscles in response to sepsis and that this activation is blocked in Atg7$^{iSkM-KO}$ mice.

The impact of sepsis and muscle-specific inactivation of autophagy on body mass, body composition, disease severity, and mortality

Although female and male Atg7$^{iSkM-KO}$ mice appeared phenotypically normal prior to sham and CLP surgical procedures, their body mass were lower compared to age-matched Atg7$^{f/f}$ mice (Figures S5A and S5B). These lower body mass cannot be attributed to the tamoxifen diet alone since wild-type mice that had been fed the same diet were relatively heavier (Figure S5A). The effect is mainly due to a decrease in lean body mass (Figure S5C), yet despite having less lean body mass, the Atg7$^{iSkM-KO}$ mice had similar *in vivo* muscle grip strength as compared to Atg7$^{f/f}$ mice (Figure S5D and S5E). Both female and male mice lost body mass in response to 48 h of sepsis, an effect which was more pronounced in Atg7$^{iSkM-KO}$ mice than in Atg7$^{f/f}$ mice (Figure 2A). Since male and female Atg7$^{f/f}$ mice and Atg7$^{iSkM-KO}$ displayed comparable loss of body mass (Figure 2A), and, as will be detailed in the following text, comparable loss of muscle mass and contractile impairment in response to sepsis, subsequent analyses were either performed on male or female mice to minimize the number of animals used while limiting variability in the data. Details on the sex of the animal are available in the Figures or Figure legends.

We next determine the effects of sustained autophagy inactivation on sepsis-induced changes in body composition, clinical signs of sepsis, and survival rates over 6 days following the sham surgery or CLP procedure. Sham Atg7$^{f/f}$ and Atg7$^{iSkM-KO}$ mice showed relatively mild body mass loss one day post-surgery, but body mass remained unchanged thereafter (Figure 2B). Both Atg7$^{f/f}$ and Atg7$^{iSkM-KO}$ mice progressively lost body mass in response to sepsis. However, body mass loss was more pronounced in septic Atg7$^{iSkM-KO}$ mice because they experienced greater losses in lean body mass as compared to Atg7$^{f/f}$ mice over a 6-day period (Figure 2C). Sepsis-induced losses of whole-body fat were similar in both groups of mice (Figure 2D). Sham Atg7$^{f/f}$ and Atg7$^{iSkM-KO}$ mice showed no signs of sickness at any point following the surgery (Figure 2E). In response to sepsis, Atg7$^{iSkM-KO}$ mice exhibited more clinical signs of illness as compared to Atg7$^{f/f}$ mice. These differences became more apparent 72 h post-CLP (Figure 2E). While no mortality was observed in sham Atg7$^{f/f}$ or Atg7$^{iSkM-KO}$ mice, survival rates in the 6-day period post-CLP were lower for Atg7$^{iSkM-KO}$ mice than for Atg7$^{f/f}$ mice (65% vs. 23%, respectively) (Figure 2F). These data collectively indicate that autophagy inactivation in skeletal muscles exacerbates the impact of sepsis on body and lean mass loss and worsens sepsis-induced mortality.

The impact of sepsis and muscle-specific inactivation of autophagy on fiber atrophy

The effects of autophagy inactivation and sepsis on muscle atrophy and contractile performance were quantified at various time points by measuring muscle mass, fiber type composition, and fiber size of the TA and GAS muscles and by measuring *in-situ* contractility of the TA. TA and GAS mass were lower in sham Atg7$^{iSkM-KO}$ mice as compared to sham Atg7$^{f/f}$ mice; this difference was independent of sex (Figures 3A and B). The TA and GAS masses were lower in CLP Atg7$^{f/f}$ and CLP Atg7$^{iSkM-KO}$ mice as compared to corresponding sham mice 48 h after the CLP procedure (Figures 3A and 3B). The TA and GAS masses in CLP Atg7$^{iSkM-KO}$ mice as compared to Atg7$^{f/f}$ mice 48 h after the CLP procedure
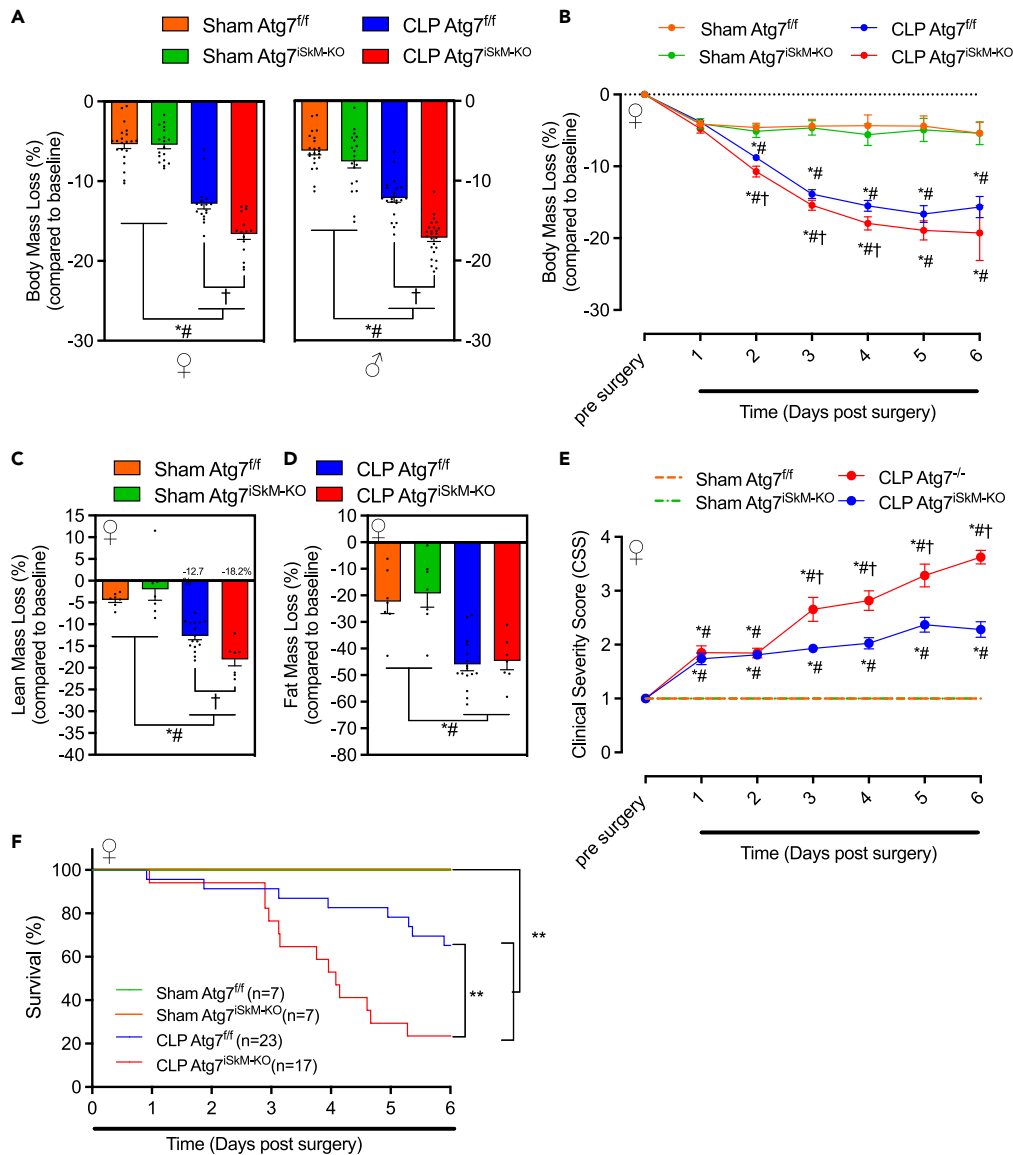
Figure 2. Autophagy inactivation exacerbates disease severity

(A) Percent change in body mass of female (left panel) and male (right panel) Atg7$^{f/f}$ and Atg7$^{iSkM-KO}$ mice in response to acute sepsis. Body mass measured prior to sham surgery or CLP then 48 h later.

(B) Percent change in body mass of female Atg7$^{f/f}$ and Atg7$^{iSkM-KO}$ mice in response to prolonged sepsis. Body mass measured prior to sham surgery or CLP then daily over a 6-day period.

(C and D) Percent change in lean (C) and fat (D) muscle mass of female Atg7$^{f/f}$ and Atg7$^{iSkM-KO}$ mice in response to prolonged sepsis. Mass measured prior to sham surgery or CLP then daily over a 4-day period.

(E) Clinical severity score (CSS) for female Atg7$^{f/f}$ and Atg7$^{iSkM-KO}$ mice in response to prolonged sepsis. CSS measured prior to sham surgery or CLP then daily over a 6-day period.

(F) Percent survival of female Atg7$^{f/f}$ and Atg7$^{iSkM-KO}$ mice in response to prolonged sepsis. Survival was monitored over a 6-day period following sham surgery or CLP. No mortality of sham Atg7$^{iSkM-KO}$ mice was observed. Comparisons of curves indicated by $**p < 0.001$. Data in panels A–E are presented as mean $\pm$ SEM. Number of animals indicated in bars, where applicable. $*p < 0.05$ vs. sham Atg7$^{f/f}$; $\#p < 0.05$ for sepsis effect (i.e., sham Atg7$^{f/f}$ vs. CLP Atg7$^{f/f}$ or sham Atg7$^{iSkM-KO}$ vs. CLP Atg7$^{iSkM-KO}$); $\dagger p < 0.05$ for sepsis plus knockout effect (i.e., CLP Atg7$^{f/f}$ vs. CLP Atg7$^{iSkM-KO}$).

(Figures 3A and 3B). Neither autophagy inactivation nor sepsis had any effect on muscle fiber type composition (Figures S5F–S5H). TA fiber diameter in sham Atg7$^{iSkM-KO}$ mice was smaller vs. sham Atg7$^{f/f}$ mice (Figures 2C–2E and 6A–6D). Forty-eight hours post sham or CLP procedure, the TA fiber diameters in
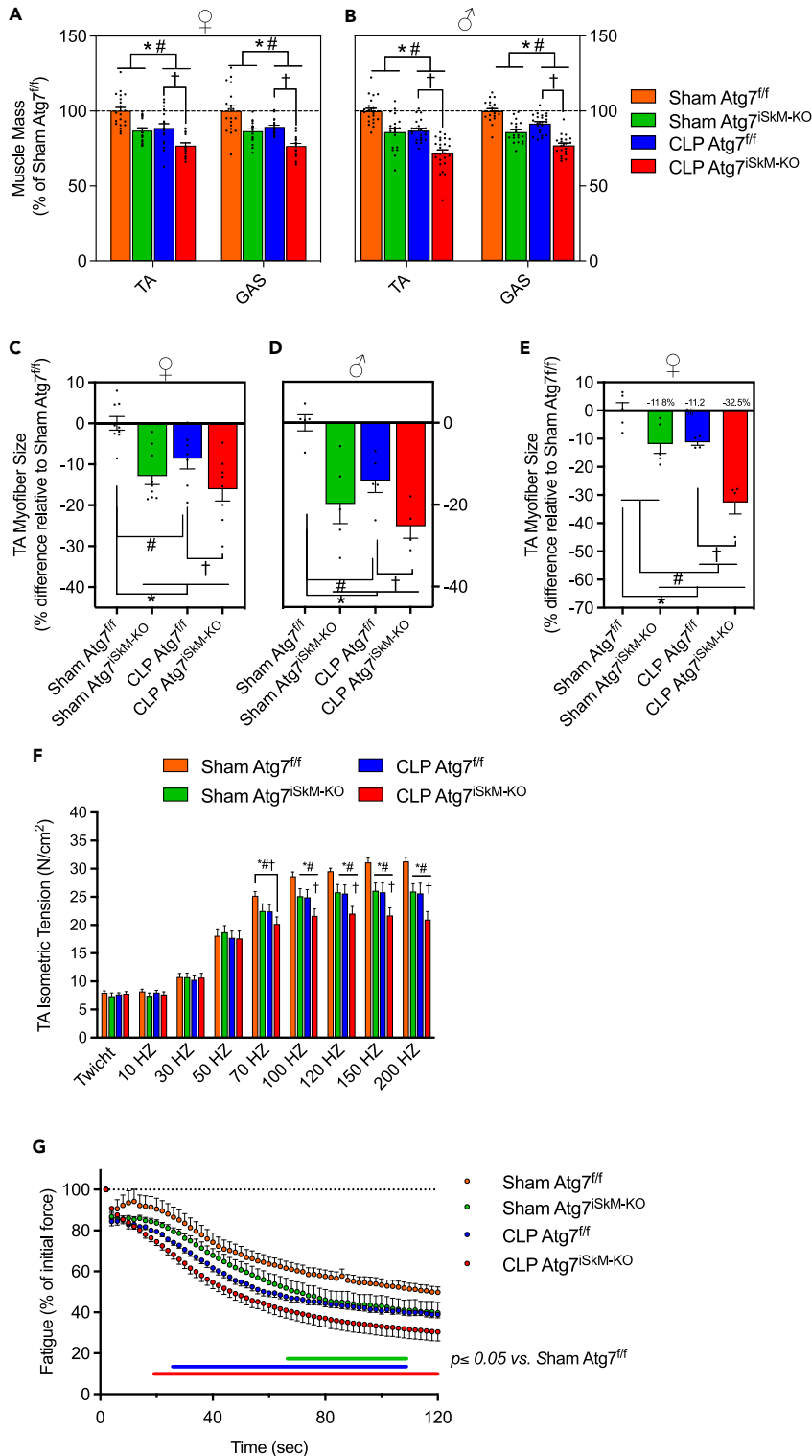
Figure 3. Impact of 48 h of sepsis on skeletal muscle mass, myofiber fiber size, and contractility

(A and B) Muscle mass loss in TA and GAS muscles of female (A) and male (B) Atg7$^{f/f}$ and Atg7$^{iSkM-KO}$ mice 48 h after sham surgery or CLP. Data are presented as percent change relative to sham Atg7$^{f/f}$ mice.

(C–E) Myofiber size of TA muscles of female (C and E) and male (D) Atg7$^{f/f}$ and Atg7$^{iSkM-KO}$ mice 48 h (C and D) or 6 days (E) after sham surgery or CLP.

Figure 3. *Continued*

(F) Isometric tension of TA muscles of female and male Atg7$^{f/f}$ and Atg7$^{iSkM-KO}$ mice 48 h after sham surgery or CLP. N = 20–23 per group).

(G) Fatigue in TA muscles of female Atg7$^{f/f}$ and Atg7$^{iSkM-KO}$ mice 48 h after sham surgery or CLP. Fatigue curves presented as percent change from tetanus 1 (initial force) to tetanus 60, n = 17 of anima, sham Atg7$^{f/f}$; n = 14, sham Atg7$^{iSkM-KO}$; n = 11, CLP Atg7$^{f/f}$; n = 12, CLP Atg7$^{iSkM-KO}$. Data in panels A–G are presented as mean $\pm$ SEM. Number ls indicated in bars, where applicable. *p < 0.05 vs. sham Atg7$^{f/f}$; #p < 0.05 for sepsis effect (i.e., sham Atg7$^{f/f}$ vs. CLP Atg7$^{f/f}$ or sham Atg7$^{iSkM-KO}$ vs. CLP Atg7$^{iSkM-KO}$); †p < 0.05 for sepsis plus knockout effect (i.e., CLP Atg7$^{f/f}$ vs. CLP Atg7$^{iSkM-KO}$).

Atg7$^{f/f}$ and Atg7$^{iSkM-KO}$ mice were lower relative to sham Atg7$^{f/f}$ mice and lower in CLP Atg7$^{iSkM-KO}$ mice relative to CLP Atg7$^{f/f}$ mice (Figures 3C and 3D). The average TA fiber diameter measured 6 days post-surgery indicated that sepsis-induced fiber atrophy was more severe in Atg7$^{iSkM-KO}$ mice vs. Atg7$^{f/f}$ mice (Figures 3E and 4D). These results collectively demonstrate that autophagy inactivation does not prevent sepsis-induced muscle atrophy in the acute septic phase of sepsis and even worsens muscle atrophy 6 days post sepsis induction.

In line with our muscle mass and fiber size data, peak isometric tension was lower in the TA muscles of sham Atg7$^{iSkM-KO}$ mice than it was in sham Atg7$^{f/f}$ mice (Figures 3F and 7A–7D). In septic muscles 48 h post CLP induction, peak isometric tension was lower in Atg7$^{f/f}$ and Atg7$^{iSkM-KO}$ mice than it was in corresponding sham mice, and lower in Atg7$^{iSkM-KO}$ mice than it was in Atg7$^{f/f}$ mice (Figure 3F). These differences in contractility were not a consequence of the tamoxifen diet per se, as peak isometric tension was lower in septic muscles of Atg7$^{iSkM-KO}$ mice than in septic muscles of WT tamoxifen-fed mice (Figure S7E). TA fatigability was assessed by subjecting muscles to 60 repeated isometric contractions with 2 s between contractions (120s total duration). The TA muscle tension progressively decreased in all mice. The fatigue effect was greater in sham Atg7$^{iSkM-KO}$ mice than it was in sham Atg7$^{f/f}$ mice (60 and 50% of initial tension at 120s, respectively) (Figure 3G), and greater in CLP Atg7$^{f/f}$ and CLP Atg7$^{iSkM-KO}$ mice than it was in corresponding sham mice (Figure 3G). These results demonstrate that autophagy is essential to the maintenance of skeletal muscle contractility and that its inactivation does not prevent sepsis-induced muscle contractile dysfunction.

The impact of sepsis and muscle-specific inactivation of autophagy on mitochondrial integrity and function

Since mitochondrial dysfunction have been implicated in the sepsis-induced skeletal muscle atrophy and weakness,[28] we next examined whether autophagy inhibition and sepsis triggered mitochondrial dysfunction in permeabilized myofibers prepared from the gastrocnemius muscle. To this end, mitochondrial respiration, H_2O_2 emission, and calcium retention capacity were assessed 48 h post sham or CLP surgery. No differences in state II (basal, ADP-restricted respiration) mitochondrial respiration were detected across groups (Figure 4A). State III mitochondrial respiration (maximal ADP-stimulated) driven by complex I substrates (glutamate plus malate) was 14% lower in septic muscles of Atg7$^{f/f}$ mice as compared to corresponding sham mice, and lower in sham and septic Atg7$^{iSkM-KO}$ mice as compared to corresponding Atg7$^{f/f}$ mice (Figure 4A). Mitochondrial coupling efficiency did not appear altered by Atg7 deletion or sepsis since no differences were observed in acceptor control ratios (ARC) (State III/State II respiration) (Figure 4B). Immunoblotting for representative subunits of the oxidative phosphorylation (OXPHOS) pathway showed that there was an overall increase in OXPHOS proteins in Atg7$^{iSkM-KO}$ mice as compared to Atg7$^{f/f}$ mice (Figure 4C). This effect is unlikely to be a result of an increase in mitochondrial biogenesis since PGC1α expression was similar in all groups (Figure 4D). To assess whether inactivation of autophagy resulted in accumulation of dysfunctional and/or damaged mitochondria, we then looked for ultrastructural abnormalities by transmission electron microscopy in GAS muscles of Sham Atg7$^{iSkM-KO}$ and CLP Atg7$^{iSkM-KO}$ mice. As expected, abnormal mitochondria with disorganized cristae and major ultrastructural abnormalities were detected in autophagy deficient skeletal muscles (Figure S8A). This is consistent with previous observations that autophagy inactivation results in the accumulation of abnormal mitochondria and autophagic vesicles, consistent with blockage of autophagy.[27,30–33]

The time to mitochondrial permeability transition pore (mPTP) opening was 12% shorter in muscles of sham Atg7$^{iSkM-KO}$ relative to sham Atg7$^{f/f}$ mice, indicating that autophagy ablation sensitized mitochondrial to mPTP opening. In Atg7$^{f/f}$ mice, 48 h of sepsis resulted in a decrease in the time to mPTP opening (Figure 4E). In Atg7$^{iSkM-KO}$ mice, 48 h of sepsis did not further shorten the time to mPTP opening (Figure 4E). These results indicate that both autophagy inactivation and sepsis enhance the susceptibility to mPTP opening
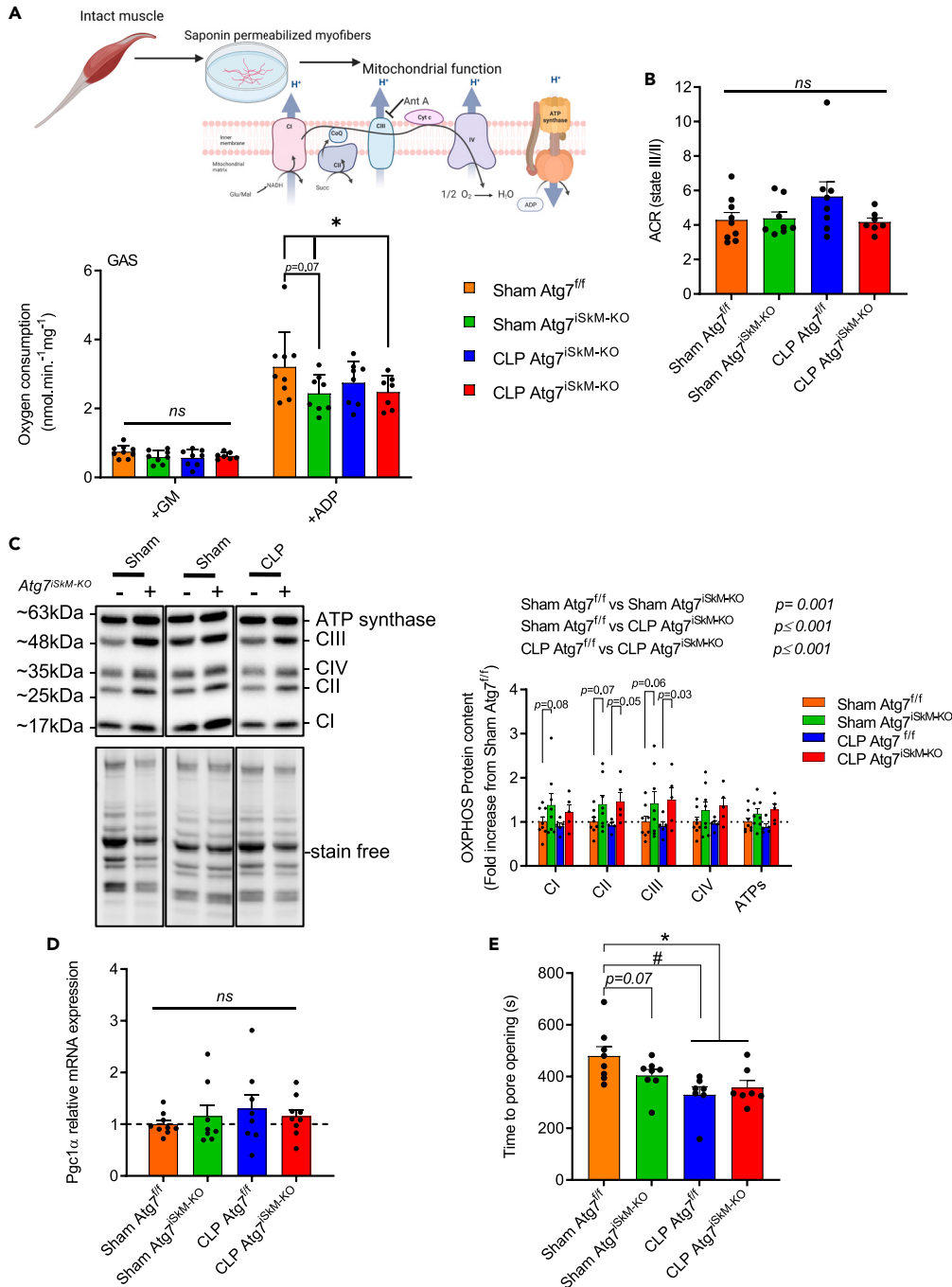
Figure 4. Impact of autophagy inactivation and sepsis on mitochondrial content and function

(A) Mitochondrial oxygen consumption in permeabilized myofibers from GAS muscles of female Atg7$^{f/f}$ and Atg7$^{iSkM-KO}$ mice 48 h after sham surgery or CLP. Data normalized per mg of muscle.

(B) Acceptor control ratio (ACR) (index of mitochondrial coupling efficiency) in GAS muscles of female Atg7$^{f/f}$ and Atg7$^{iSkM-KO}$ mice 48 h after sham surgery or CLP.

(C) Representative immunoblots of respiratory chain subunits (OXPHOS) in GAS muscles of female Atg7$^{f/f}$ and Atg7$^{-/-}$ mice 48 h after sham surgery or CLP (n = 8 for each sham group, n = 5 each CLP group). Stain-free technology was used to normalize subunits. Significant increases in sham and septic Atg7$^{iSkM-KO}$ mice suggest accumulation of impaired mitochondria.

(D) mRNA expression of PGC1α in TA muscles of male Atg7$^{f/f}$ and Atg7$^{-/-}$ mice 48 h after sham surgery or CLP (n = 6-8 per group).

Figure 4. Continued

(E) Time of opening of the mPTP in permeabilized myofibers from GAS muscles of female Atg7$^{f/f}$ and Atg7$^{iSkM-KO}$ mice 48 h after sham surgery or CLP. Number of animals indicated in bars, where applicable. *p < 0.05 vs. sham Atg7$^{f/f}$; #p < 0.05 for sepsis effect (i.e., sham Atg7$^{f/f}$ vs. CLP Atg7$^{f/f}$ or sham Atg7$^{iSkM-KO}$ vs. CLP Atg7$^{iSkM-KO}$); †p < 0.05 for sepsis plus knockout effect (i.e., CLP Atg7$^{f/f}$ vs. CLP Atg7$^{iSkM-KO}$).

in skeletal muscles. Yet, despite significant changes in mitochondrial respiratory capacity and mPTP opening time, there were no significant effects of autophagy inactivation nor sepsis on mitochondrial hydrogen peroxide (H_2O_2) production (Figure S8B).

The impact of 48 h of sepsis and muscle-specific inactivation of autophagy on the ubiquitin-proteasome pathway and protein synthesis

Previous studies have shown that inactivation of autophagy in skeletal muscles triggers significant increases in 26S proteasome activity.[27] To determine if this occurred in the skeletal muscles of Atg7$^{iSkM-KO}$ mice, ubiquitin E3 ligase expressions and 11S, 19S, and 20S subunits of the 26S proteasome were measured 48 h post-surgery in the TA and GAS of sham-operated and septic animals. No significant differences in the expressions of tripartite motif containing 32 (*Trim32*), *Nedd4*, *Fbxo32*, *Fbxo30* (Musa1), and *Trim63* were observed between sham Atg7$^{f/f}$ and Atg7$^{iSkM-KO}$ mice, nor were any observed for proteasome 26S subunits *Psmd11* and *Psmd8* (19S) or the constitutive and inducible β subunits of 20S (Figures 5A–5E, S9A, and S9B). However, two 11S subunits, proteasome activator subunits 1 and 2 (*Psme1* and *Psme2*), one constitutive 20S subunits of 20S, subunit beta 5 (*Psmb5*) and one 20S β subunit, proteasome 20S subunit beta 10 (*Psmb10*), were upregulated in Atg7$^{iSkM-KO}$ mice, relative to Atg7$^{f/f}$ mice (Figures 5B and 5E).

In sepsis, *Fbxo30*, *Fbxo32*, *Trim63*, *Psmd11*, *Psmd8*, and 2 constitutive 20S subunits of 20S, subunit beta 2 and 5 (*Psmb7*, *Psmb5*), were upregulated in Atg7$^{f/f}$ and Atg7$^{iSkM-KO}$ mice as compared to corresponding sham mice (Figures 5A–5E and S9A–S9C). Furthermore, sepsis increased total protein ubiquitination levels in both Atg7$^{f/f}$ and Atg7$^{iSkM-KO}$ mice (Figures 5H and 5I). Protein ubiquitination levels were also higher in muscles of sham Atg7$^{iSkM-KO}$ relative to sham Atg7$^{f/f}$ mice (Figures 5F and 5G).

Because skeletal muscle mass is regulated by the balance between protein synthesis and degradation, we measured *in vivo* protein synthesis using SUnSET method.[34] No significant differences in the rate of protein synthesis were observed across all groups (Figures S9D and S9E). Collectively, these results suggest that autophagy inactivation in skeletal muscles coincides with increased activity of specific subunits of the 26S proteasome but does not affect the expression of ubiquitin E3 ligases or protein synthesis. Sepsis, in contrast, does trigger upregulation of the E3 ligases, as well as specific subunits of the 19S and 20S proteasome, but does not seem to suppress protein synthesis.

Potential mechanisms underlying the prolonged effects of autophagy inactivation on sepsis-induced muscle dysfunction

Following prolonged sepsis (6 days post CLP surgery), Atg7$^{iSkM-KO}$ mice developed severe limb muscle fiber atrophy vs. Atg7$^{f/f}$ mice. To determine why, transcriptomic analyses were performed on TA samples from Atg7$^{f/f}$ and Atg7$^{iSkM-KO}$ mice 6 days after sepsis was induced. In Atg7$^{iSkM-KO}$ mice, 451 genes were upregulated and 323 were downregulated in comparison to Atg7$^{f/f}$ mice (FDR-adjusted p < 0.05; Figure 6A). Gene ontology (GO) analyses of differentially expressed genes indicate that cellular processes such as catabolism, stress response, ribonucleoprotein synthesis, and intracellular protein transport were highly augmented in septic muscles Atg7$^{iSkM-KO}$ mice (Figure 6B). Catabolism-associated genes involved in muscle atrophy were highly upregulated, including *Trim63*, *Fbxo32*, and *Fbxo31* and *Psma3*, *Psma4*, *Psma5*, *Psma7*, *Psmb2*, *Psmb4*, *Psmb6*, *Psmc2*, *Psmc3*, *Psmc5*, *Psmd1*, and *Psmd11* (Figure S10A). Ingenuity pathway analysis (IPA) of differentially expressed genes demonstrated that several molecular networks were upregulated in Atg7$^{iSkM-KO}$ mice as compared to Atg7$^{f/f}$ mice in response to sepsis (Table S1). This indicates that strong activation of the ubiquitin proteasome proteolytic pathway is triggered in muscles in which the essential autophagy gene *Atg7* has been deleted, and that this activation may lead to more severe atrophy than when it has not been deleted.

FoxO transcription factors are major regulators of the autophagy and proteasome proteolytic pathways.[18,35] They transcribe several autophagy-related genes, ubiquitin E3 ligases, and proteasome subunits. To determine the degree to which they were activated in response to autophagy inactivation and sepsis,
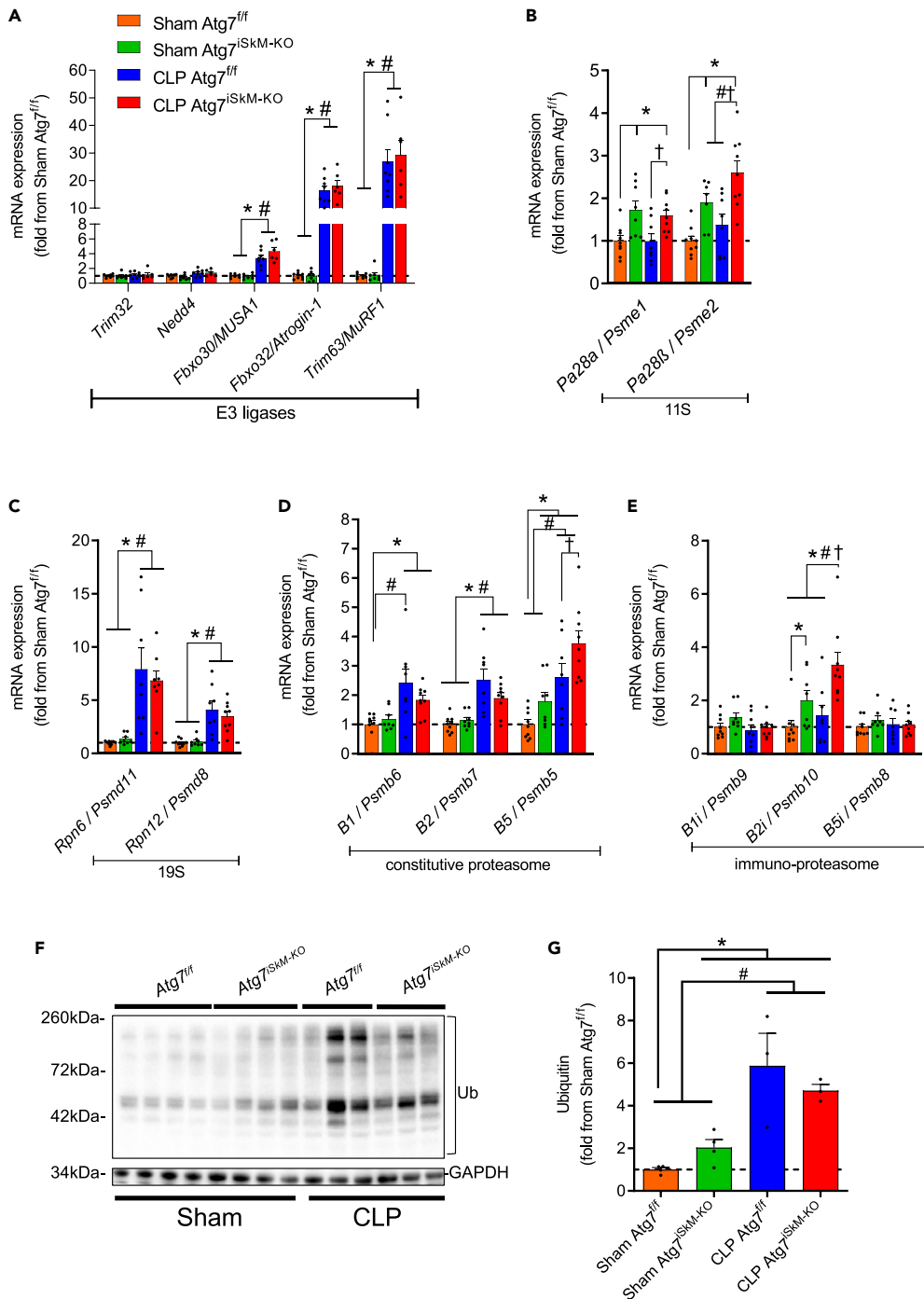
Figure 5. Impact of autophagy inactivation and sepsis on markers of the ubiquitin-proteasome pathway

(A) mRNA expressions of E3 ubiquitin ligases in TA muscles of female Atg7$^{f/f}$ and Atg7$^{iSkM-KO}$ mice 48 h after sham surgery or CLP.

(B–E) mRNA expressions of proteasome subunits genes in TA muscles of female Atg7$^{f/f}$ and Atg7$^{iSkM-KO}$ mice 48 h after sham surgery or CLP. 18S levels used as a control. As fold change relative to sham Atg7$^{f/f}$.

(F–G) Representative immunoblot and quantification of ubiquitinated protein levels in TA muscle of female Atg7$^{f/f}$ and Atg7$^{iSkM-KO}$ mice 48 h after sham surgery or CLP. GAPDH serves as loading control. Data in panels A–E and G are presented as mean ± SEM. *p < 0.05 vs. sham Atg7$^{f/f}$; #p < 0.05 for sepsis effect (i.e., sham Atg7$^{f/f}$ vs. CLP Atg7$^{f/f}$ or sham Atg7$^{iSkM-KO}$ vs. CLP Atg7$^{iSkM-KO}$); †p < 0.05 for sepsis plus knockout effect (i.e., CLP Atg7$^{f/f}$ vs. CLP Atg7$^{iSkM-KO}$).
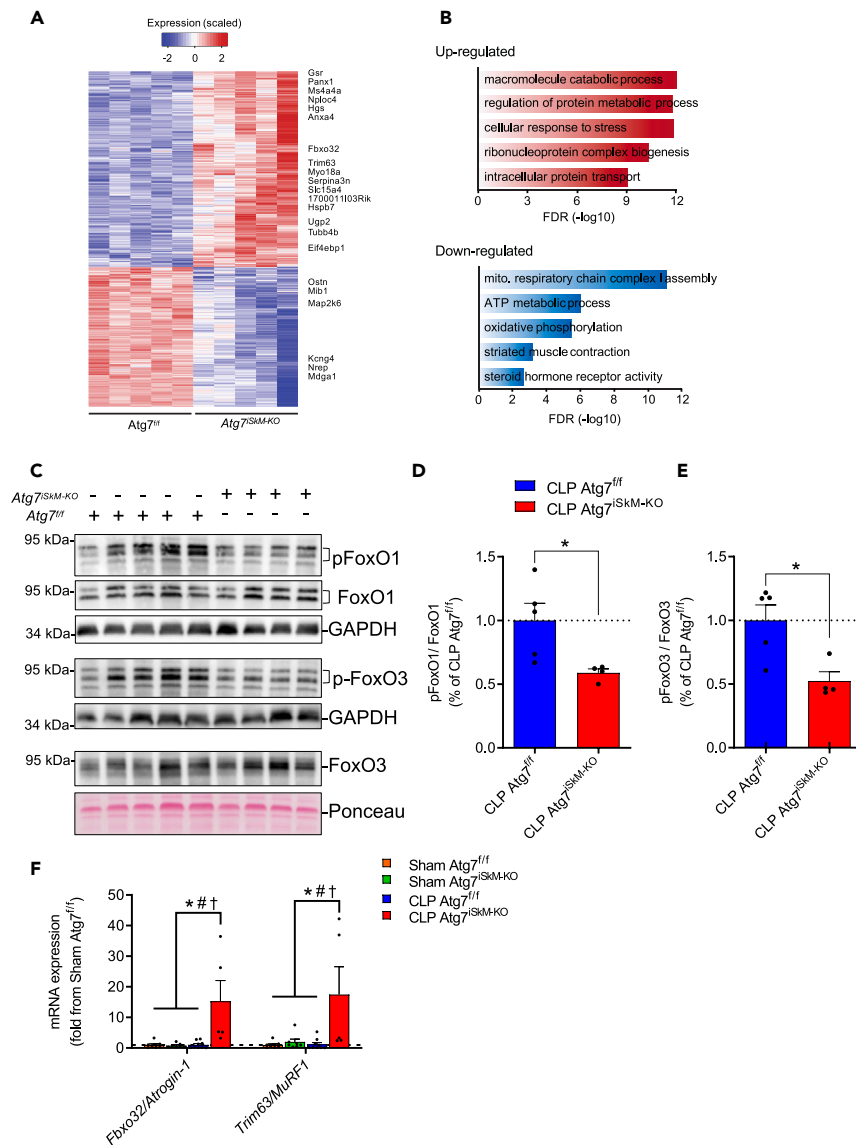
Figure 6. Effects of prolonged sepsis and autophagy inactivation on skeletal muscle transcriptome

(A) Heatmap showing skeletal muscle gene expression signatures in $Atg7^{f/f}$ and $Atg7^{iSkM-KO}$ mice in response to prolonged sepsis (6 days). Colors indicate relative expression levels; red indicates high expression and blue indicates low expression.

(B) Top five upregulated and downregulated pathways as identified through biometric analyses. FDR = false discovery ratio.

(C) Representative immunoblots of pFoxO1, FoxO1, pFoxO3, and FoxO3 protein levels in TA skeletal muscles of female $Atg7^{f/f}$ and $Atg7^{iSkM-KO}$ mice 6 days after CLP showing decreased phosphorylation of FoxO1 and FoxO3 resulting from Atg7 knockout and sepsis.

(D and E) Densitometric analyses of pFoxO1 and pFoxO3 proteins normalized to GAPDH in $Atg7^{f/f}$ and $Atg7^{iSkM-KO}$ mice 6 days after CLP. GAPDH or Ponceau serves as loading control. Number of animals indicated within bars. Data are presented as mean $\pm$ SEM. Knockout effect indicated by *$p < 0.05$, CLP $Atg7^{f/f}$ vs. CLP $Atg7^{iSkM-KO}$.

(F) mRNA expressions of E3 ubiquitin ligases in TA muscles of female $Atg7^{f/f}$ and $Atg7^{iSkM-KO}$ mice 6 days after sham surgery or CLP. 18S levels used as a control. Data are presented as fold change relative to sham $Atg7^{f/f}$ and as mean $\pm$ SEM, n = 5–8 per group. *$p < 0.05$ vs. sham $Atg7^{f/f}$; #$p < 0.05$ for sepsis effect (i.e., sham $Atg7^{f/f}$ vs. CLP $Atg7^{f/f}$ or sham $Atg7^{iSkM-KO}$ vs. CLP $Atg7^{iSkM-KO}$); †$p < 0.05$ for sepsis plus knockout effect (i.e., CLP $Atg7^{f/f}$ vs. CLP $Atg7^{iSkM-KO}$).

FOXO1 and FOXO3 phosphorylation levels were quantified in the TA muscles of Atg7$^{f/f}$ and Atg7$^{iSkM-KO}$ mice. In response to sepsis, the phosphorylation of both transcription factors was strongly attenuated in Atg7$^{iSkM-KO}$ mice as compared to Atg7$^{f/f}$ mice (Figures 6C–6E). *Fbxo32* and *Trim63* were also induced in Atg7$^{iSkM-KO}$ mice, but not in Atg7$^{f/f}$ mice, where levels remained like those detected in sham mice (Figure 6F). These results show that the ubiquitin proteasome pathway is sustainably activated in response to prolonged sepsis when autophagy has been inactivated.

Transcriptome analyses showed that several cellular processes, such as mitochondrial respiratory chain complex assembly, ATP metabolism, OXPHOS, muscle contraction, and steroid hormone receptor activity, were downregulated in response to sepsis in the TA of Atg7$^{iSkM-KO}$ mice as compared to septic Atg7$^{f/f}$ mice (Figure 6B). Downregulated genes associated with mitochondrial metabolism included NADH: ubiquinone oxidoreductase subunits S8, S5, S4, B7, B2, and B11 (*Ndufs8*, *Ndufs5*, *Ndufs4*, *Ndufb7*, *Ndufb2*, and *Ndufb11*), NADH: ubiquinone oxidoreductase complex assembly factors 6, 5, 9, 13, 11, and 1 (*Ndufaf6*, *Ndufaf5*, *Ndufa9*, *Ndufa13*, *Ndufa11*, and *Ndufa1*) (Figure S10B). A full list of differentially regulated gene and pathway analyses are listed in Table S1. Collectively, these results suggest that inactivation of autophagy intensifies the negative repercussions that sepsis exerts on a number of processes that are critical to skeletal muscle contractile function, as well as enhancing activation of the proteasome proteolytic pathway, resulting in worsened muscle fiber atrophy.

The impact of sepsis and muscle-specific inactivation of autophagy on whole-body metabolism and energy balance

To evaluate the regulatory role of skeletal muscle autophagy in relation to whole body metabolism, indirect calorimetry was performed before and after surgery. Before surgery, no differences in respiratory exchange ratio (RER), rate of oxygen consumption (VO$_2$), heat production, feeding behavior, non-fasting blood glucose, body temperature, and whole-body fatty acid oxidation were found between Atg7$^{f/f}$ and Atg7$^{iSkM-KO}$ mice, despite the latter having lower total movement (Figure S11). On Day 1 post-surgery, total VO$_2$ decreased in response to sepsis in Atg7$^{f/f}$ and Atg7$^{iSkM-KO}$ mice, and recovered to pre-surgical values thereafter (Figure 7A).

RER in sham Atg7$^{f/f}$ and Atg7$^{iSkM-KO}$ mice declined 1-day post-surgery, with complete recovery thereafter (Figures 7B and 7C). These transient declines were coincident with decreased food intake (Figure 7D). In response to sepsis, RERs in Atg7$^{f/f}$ and Atg7$^{iSkM-KO}$ mice persistently declined, suggesting increased dependence on lipid oxidation, which is consistent with reductions in food intake, although no differences in intake were observed (Figures 7B–7D). This suggests that the different rates of mass loss that occurred in these mice were not a consequence of variability in food intake (Figures 2A and 2B). Persistent decrease in total movement was observed in both Atg7$^{f/f}$ and Atg7$^{iSkM-KO}$ mice in response to sepsis, an effect that was more severe in Atg7$^{iSkM-KO}$ than Atg7$^{f/f}$ mice (Figure 7E). Heat production decreased in Atg7$^{f/f}$ and Atg7$^{iSkM-KO}$ mice in response to sepsis only on Day 1 post-surgery (Figure 7F).

It has been well established that body temperature is a strong predictor of mortality during critical illness[36–38] and that skeletal muscles play a major role in thermogenesis.[39,40] To identify the mechanisms underlying mass loss and increased lethality of Atg7$^{iSkM-KO}$ mice in response to sepsis, we monitored rectal temperature, blood glucose, and β-hydroxybutyrate levels. Autophagy ablation in sham operated mice had no impact on rectal temperature. While sepsis had a modest impact on rectal temperature in Atg7$^{f/f}$ mice, it led to a progressive decline in rectal temperature in Atg7$^{iSkM-KO}$ mice (Figure 8A). Blood glucose levels in sham Atg7$^{f/f}$ and Atg7$^{iSkM-KO}$ mice declined on Day 1 post-surgery and remained lower than pre-surgery values for the duration of the experimental period (Figure 8B). Blood glucose levels were lower in Atg7$^{f/f}$ and Atg7$^{iSkM-KO}$ mice in response to sepsis as compared to corresponding sham mice, and even lower in Atg7$^{iSkM-KO}$ mice as compared to Atg7$^{f/f}$ mice, up until Day 6 post-surgery (Figure 8B). These findings are consistent with previous results demonstrating the importance of muscle autophagy in the regulation of glucose levels during fasting.[41] Blood β-hydroxybutyrate levels were elevated in response to sepsis in both Atg7$^{f/f}$ and Atg7$^{iSkM-KO}$ mice, although to a greater degree in Atg7$^{iSkM-KO}$ mice (Figure 8C). These results suggest that increased ketogenesis compensates for hypoglycemia and that the absence of muscle autophagy worsens sepsis-induced hypoglycemia and hyperketonemia.
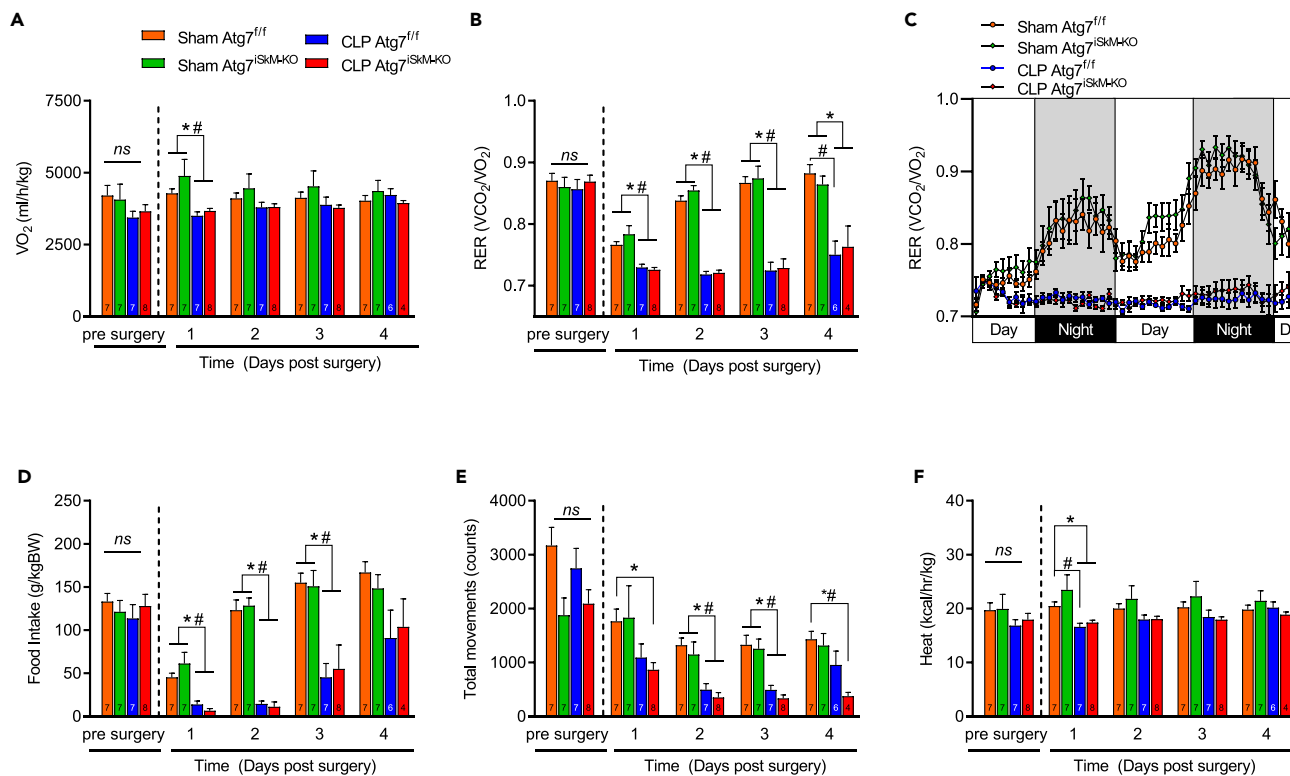
Figure 7. Effects of autophagy inactivation and sepsis on food intake, energy expenditure and substrate utilization

(A–C) Average kinetic data for whole-body oxygen consumption (VO_2) and RER (VCO_2/VO_2) during day and night periods over a 48-h period after sham surgery or CLP. D) Food intake (gram of consumed food per kg of body mass per day.

(E) Total movement (ambulatory activity).

(F) Heat (energy expenditure) relative to daily body mass. Metabolic parameters measured by indirect calorimetry for 2 days prior to surgery and 4 days after sham surgery or CLP. Food intake and metabolic parameters expressed relative to daily body mass, given differences in body composition over time. PhenoMaster metabolic cage data measured on a dark (6:00 p.m. to 6:00 a.m.)/light (6:00 a.m. to 6:00 p.m.) cycle. Data are presented as mean $\pm$ SEM. *$p < 0.05$ vs. sham Atg7$^{f/f}$; #$p < 0.05$ for sepsis effect (i.e., sham Atg7$^{f/f}$ vs. CLP Atg7$^{f/f}$ or sham Atg7$^{iSkM-KO}$ vs. CLP Atg7$^{iSkM-KO}$); †$p < 0.05$ for sepsis plus knockout effect (i.e., CLP Atg7$^{f/f}$ vs. CLP Atg7$^{iSkM-KO}$).

DISCUSSION

To date, the functional importance of autophagy in sepsis-induced skeletal muscle dysfunction has not been fully elucidated. In a recent report, we demonstrated that the molecular machinery of autophagy in skeletal muscle fibers is strongly activated by sepsis.[13] In the current study, we used tamoxifen-inducible skeletal muscle-specific Atg7 knockout (Atg7$^{iSkM-KO}$) mice to determine whether autophagy inactivation is protective of or detrimental to muscle function and atrophy in septic mice. We demonstrate for the first time how important autophagy is to the regulation of skeletal muscle integrity over the course of a critical illness like sepsis. We show that *Atg7* deletion selectively in skeletal muscles does not prevent skeletal muscle atrophy and weakness during sepsis. Rather, it accelerates losses of muscle mass, myofiber atrophy, and whole-body lean mass over a 6-day period.

With the aim of identifying the mechanism underlying the more severe atrophy observed in Atg7$^{iSkM-KO}$ mice in response to sepsis, we reasoned that the severity of sepsis-induced muscle atrophy might be explained by the upregulation of the proteasome proteolytic system since this system contributes to a large extent to the degradation of muscle proteins including myofilament proteins.[42–45] Consistent with previous work from our laboratory which showed significant activation of the proteasome proteolytic pathway in septic skeletal muscles,[13] we report that sepsis was associated with significant upregulation of two muscle-specific ubiquitin E3 ligases *Fbxo32* and *Trim63*. Interestingly, the expression of these two ubiquitin E3 ligases were comparable between Atg7$^{iSkM-KO}$ and Atg7$^{f/f}$ mice at baseline and the degrees to which were induced 48 h post sepsis were similar in Atg7$^{iSkM-KO}$ and Atg7$^{f/f}$ mice. These results suggest that
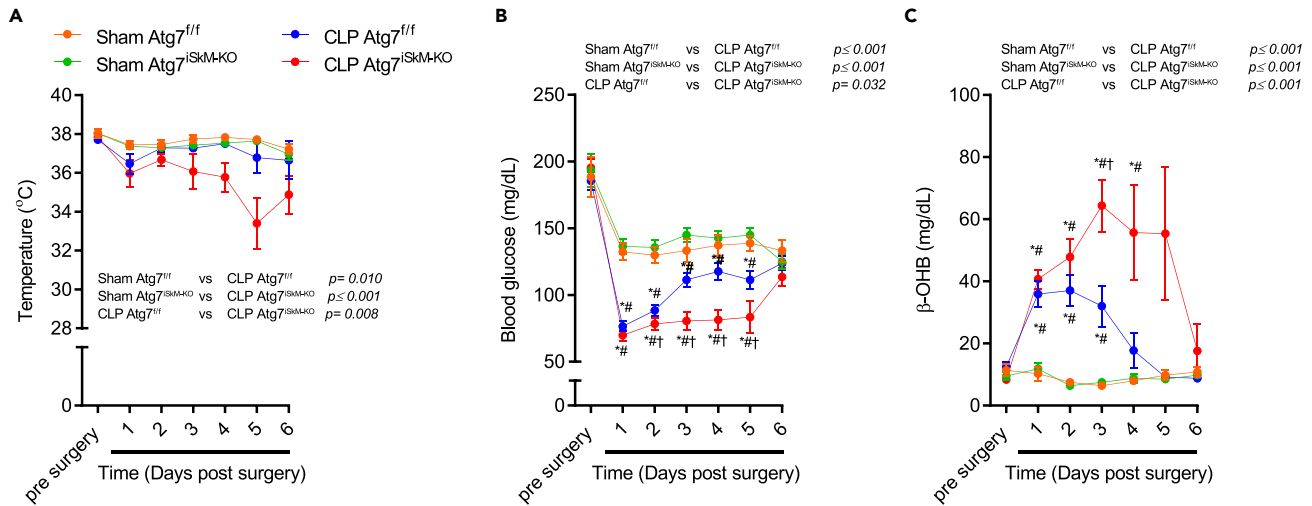
Figure 8. Autophagy inactivation in skeletal muscles exacerbates sepsis-induced metabolic impairments

(A–C) Kinetics of core body temperature B) Whole blood glucose and C) β-OHB levels measured in Atg7[f/f] and Atg7[iSkM−KO] mice over a 6-day period between 6 and 8 a.m. Data are presented as mean ± SEM. *$p < 0.05$ vs. sham Atg7[f/f]; #$p < 0.05$ for sepsis effect (i.e., sham Atg7[f/f] vs. CLP Atg7[f/f] or sham Atg7[iSkM−KO] vs. CLP Atg7[iSkM−KO]); †$p < 0.05$ for sepsis plus knockout effect (i.e., CLP Atg7[f/f] vs. CLP Atg7[iSkM−KO]).

Fbxo32 and *Trim63* do not contribute to the lower muscle mass and strength observed in Atg7[iSkM−KO] mice. However, we should point out that 6 days post sepsis initiation, the expressions of both *Fbxo32* and *Trim63* in Atg7[f/f] mice returned to normal levels while their expressions remained significantly elevated in septic Atg7[iSkM−KO] mice. These findings can be partly explained by increased activities of FoxO1 and FoxO3 transcription factors, which are known to mediate the atrophy program and the induction of *Fbxo32* and *Trim63* in catabolic conditions.[18,35] In addition to ubiquitin E3 ligases, we measured the expression of constitutive and inducible subunits of 20S, 19S, and 11S components of the 26S proteasome as indicator of the activity of the proteasome proteolytic pathway. We found that the levels of two subunits of 11S (*Psme1* and *Psme2*) and one β subunit of 20S, *Psmb10*, were significantly elevated in muscles of Atg7[iSkM−KO] mice as compared to Atg7[f/f] mice under sham and sepsis conditions (Figure 5). These results indicate for the first-time selective autophagy inactivation in normal (sham) skeletal muscles leads to compensatory increases in the expressions of various 26S proteasome subunits and that late phases of sepsis is associated with substantial induction of both ubiquitin E3 ligases and proteasome subunit expression in muscles of mice with deficient autophagy.

Our results show that muscles of sham Atg7[iSkM−KO] mice displays a significant decrease in mitochondrial respiration and a trend for a decrease in the time to mPTP opening. These results therefore strengthen the literature showing that autophagy is essential for the maintenance of optimal mitochondrial function.[27,30–33,46] In agreement with previous studies,[22,47–50] we also report that sepsis results in mitochondrial dysfunction, characterized by reduced respiration and impaired mPTP function. The results suggest that an accumulation of dysfunctional mitochondria might have contributed to sepsis-induced muscle atrophy and weakness in Atg7[f/f] mice. In line with this view, we recently reported that overexpressing Parkin, a protein regulating mitophagy, can attenuate sepsis-induced skeletal muscle wasting.[28] Surprisingly, however, mitochondrial respiration, time to mPTP opening and H_2O_2 emission were not further altered 48 h post sepsis in Atg7[iSkM−KO] mice. These data suggest that further accumulation of mitochondrial dysfunction might not have contributed to the severe atrophy and contractile dysfunction in Atg7[iSkM−KO] mice in response to sepsis. However, it should be noted that many mitochondrial genes were still downregulated 6 days post CLP in Atg7[iSkM−KO] mice, suggesting that further mitochondrial dysfunction might progressively develop past 48 h in autophagy deficient skeletal muscle.

Another important finding of our study is that sepsis was associated with stronger signs of sickness in Atg7[iSkM−KO] mice relative to Atg7[f/f] mice (Figure 2D). Indeed, Atg7[f/f] mice exhibited several sickness behaviors in response to sepsis, including loss of appetite, reduced physical activity, and severe body mass loss, resulting in a reduced survival rates (e.g., 65% survival 6 days post CLP). These behavioral abnormalities associated with sepsis have been previously reported by investigators using the CLP model of

sepsis.[51] However, a more severe sepsis phenotype was observed in Atg7[iSkM−KO] mice, characterized by more pronounced body mass loss, more severe signs of sickness, and a worse survival rate. Importantly, differences in food intake are unlikely to explain the more severe phenotype seen in response to sepsis in Atg7[iSkM−KO] mice since measurements of food intake showed no differences between the two genotypes. In the absence of differences in body fat loss between Atg7[iSkM−KO] and Atg7[f/f] mice, the more likely mechanism behind pronounced sepsis-induced body mass loss in Atg7[iSkM−KO] mice is the significantly greater skeletal muscle wasting observed in these mice relative to Atg7[f/f] mice.

We also observed that autophagy inactivation in skeletal muscle can worsen systemic metabolic derangements associated with sepsis, as reflected by more severe hyperketonemia and hypoglycemia. Ketogenesis is normally activated in response to catabolic stress to spare glucose and to support brain function.[52] Because hyperketosis can lead to ketoacidosis, which can lead to coma and death, our data, and recent observations,[53] suggest elevated β-hydroxybutyrate levels may be involved in the pathogenesis of sepsis. With respect to the more pronounced and persistent hypoglycemia that was seen in Atg7[iSkM−KO] mice, several studies have demonstrated that autophagy plays an important role in the regulation of whole-body glucose metabolism.[32,41,54] Indeed, Kim et al. recently showed that the muscle-selective deletion of Atg7 in high fat fed mice resulted in lower glycemia and protected against insulin resistance and obesity.[32] In the liver, autophagy contributes to the maintenance of glycemia through the conversion of amino acids to glucose via gluconeogenesis.[54] Indeed, in mice with liver-specific deletion of Atg7, starvation was shown to result in greater decrease in blood glucose levels as compared to wild type animal.[54] Based on these findings, we speculate that induction of autophagy in septic muscles may be particularly important in providing the amino acids that the liver requires to maintain glycemia and in eliminating damaged proteins and organelles in muscle cells, thereby limiting contractile dysfunctions and optimizing survival. One intriguing finding from the present study is the similar fat mass loss triggered by sepsis in Atg7[iSkM−KO] and Atg7[f/f] mice. Indeed, based on the major systemic metabolic defects, the worse clinical severity score and the higher mortality seen in septic Atg7[iSkM−KO] mice, one could have expected greater fat mass loss in these mice. While this similar fat mass loss seen in Atg7[iSkM−KO] and Atg7[f/f] mice in response to sepsis would require further study, it is tempting to speculate that alterations in skeletal muscle autophagy might disrupt interorgan communication during sepsis.

It should be emphasized that our findings of a protective role of autophagy against sepsis-induced skeletal muscle atrophy and contractile dysfunction and increased mortality of septic Atg7[iSkM−KO] mice relative to Atg7[f/f] mice are in agreement with previous reports indicating a protective role for autophagy against sepsis-induced organ and cellular failure in the liver and immune cells.[55–57] Indeed, selective inactivation of autophagy in the liver resulted in increased mortality, severe mitochondrial damage, and activation of apoptosis in murine sepsis models.[55,56] Similarly, selective inactivation of autophagy in T cells was associated with enhanced T cells apoptosis and increased sepsis-induced mortality.[57] Since activation of autophagy in response to sepsis plays a pivotal role in the physiological maintenance of cellular homeostasis, our study raises concerns about early nutritional and insulin therapies that may suppress autophagy in critically ill patients.

In summary, we highlight in this study that autophagy inactivation in skeletal muscles triggers significant worsening of sepsis-induced muscle atrophy and contractile dysfunction. We also provide evidence indicating that autophagy inactivation in skeletal muscles worsens sepsis-induced hypoglycemia and hyperketosis and negatively impacts survival. These results position enhancing autophagy as a potential therapeutic approach for treating sepsis-induced skeletal muscle dysfunction and metabolic derangements.

Limitations of the study

While the present study provides robust data showing that genetic ablation of autophagy specifically in skeletal muscles has major systemic impacts during sepsis, it did not identify the exact underlying mechanisms. Data presented in this study were solely derived from experiments involving preclinical mouse models. While these models have undeniable preclinical value, it should be noted that major differences in skeletal muscle physiology exist between rodents and humans.[58,59] As such, caution is warranted when extrapolating our findings to human skeletal muscles.[58] All mice used in the present study were relatively young. However, sepsis is a condition that disproportionately affects older adults.[60] Whether aging impacts the conclusions of this study will require further research.

STAR★METHODS

Detailed methods are provided in the online version of this paper and include the following:

- KEY RESOURCES TABLE
- RESOURCE AVAILABILITY
  - Lead contact
  - Materials availability
  - Data and code availability
- EXPERIMENTAL MODEL AND STUDY PARTICIPANT DETAILS
- METHOD DETAILS
  - Cecal ligation and puncture
  - *In situ* measurement of TA contractility
  - Preparation of permeabilized muscle fibers
  - Mitochondrial respiration
  - Mitochondrial H_2O_2 production
  - Mitochondrial Ca^{2+} retention capacity (CRC)
  - Transmission electron microscopy
  - Measurement of myofiber atrophy
  - p62/SQSTM1 positive myofibers
  - Assessment of fiber type composition
  - Body composition analysis
  - Grip strength assessment
  - Quantification of blood metabolites
  - Assessment of body temperature
  - Animal monitoring in metabolic cages
  - Autophagic flux quantification
  - *In vivo* protein synthesis measurements
  - Immunoblotting
  - RNA extraction and real-time PCR
  - Microarrays
- QUANTIFICATION AND STATISTICAL ANALYSIS

SUPPLEMENTAL INFORMATION

Supplemental information can be found online at https://doi.org/10.1016/j.isci.2023.107475.

AUTHOR CONTRIBUTIONS

Conceptualization, S.N.A.H., G.G., and J.P.L.G.; Methodology, S.N.A.H., M.S., G.G. and J.P.L.G.; Investigation, J.P.L.G., K.M., M.C., J.F., A.M., T.J.C., O.R., F.E.B., A.S., D.M., L.H., M.S., S.N.A.H., and G.G.; Writing—Original Draft, G.G. and J.P.L.G.; Writing—Review & Editing, S.N.A.H., G.G., and J.P.L.G.;

REFERENCES

1. Khan, J., Harrison, T.B., Rich, M.M., and Moss, M. (2006). Early development of critical illness myopathy and neuropathy in patients with severe sepsis. Neurology 67, 1421–1425. https://doi.org/10.1212/01.wnl.0000239826.63523.8e.

2. Tennilä, A., Salmi, T., Pettilä, V., Roine, R.O., Varpula, T., and Takkunen, O. (2000). Early signs of critical illness polyneuropathy in ICU patients with systemic inflammatory response syndrome or sepsis. Intensive Care Med. 26, 1360–1363. https://doi.org/10.1007/s001340000586.

3. De Jonghe, B., Sharshar, T., Hopkinson, N., and Outin, H. (2004). Paresis following mechanical ventilation. Curr. Opin. Crit. Care 10, 47–52. https://doi.org/10.1097/00075198-200402000-00008.

4. de Jonghe, B., Lacherade, J.C., Sharshar, T., and Outin, H. (2009). Intensive care unit-acquired weakness: risk factors and prevention. Crit. Care Med. 37, S309–S315. https://doi.org/10.1097/CCM.0b013e3181b6e64c.

5. Cheung, A.M., Tansey, C.M., Tomlinson, G., Diaz-Granados, N., Matté, A., Barr, A., Mehta, S., Mazer, C.D., Guest, C.B., Stewart, T.E., et al. (2006). Two-Year Outcomes, Health Care Use, and Costs of Survivors of Acute Respiratory Distress Syndrome. Am. J. Respir. Crit. Care Med. 174, 538–544. https://doi.org/10.1164/rccm.200505-693OC.

6. Tiao, G., Fagan, J.M., Samuels, N., James, J.H., Hudson, K., Lieberman, M., Fischer, J.E., and Hasselgren, P.O. (1994). Sepsis stimulates nonlysosomal, energy-dependent proteolysis and increases ubiquitin mRNA levels in rat skeletal muscle. J. Clin. Invest. 94, 2255–2264. https://doi.org/10.1172/JCI117588.

7. Supinski, G.S., and Callahan, L.A. (2010). Calpain activation contributes to endotoxin-induced diaphragmatic dysfunction. Am. J. Respir. Cell Mol. Biol. 42, 80–87. https://doi.org/10.1165/rcmb.2008-0275OC.

8. Supinski, G.S., and Callahan, L.A. (2006). Caspase activation contributes to endotoxin-induced diaphragm weakness. J. Appl. Physiol. 100, 1770–1777. https://doi.org/10.1152/japplphysiol.01288.2005.

9. Supinski, G.S., Wang, W., and Callahan, L.A. (2009). Caspase and calpain activation both contribute to sepsis-induced diaphragmatic weakness. J. Appl. Physiol. 107, 1389–1396. https://doi.org/10.1152/japplphysiol.00341.2009.

10. Hobler, S.C., Williams, A., Fischer, D., Wang, J.J., Sun, X., Fischer, J.E., Monaco, J.J., and Hasselgren, P.O. (1999). Activity and expression of the 20S proteasome are increased in skeletal muscle during sepsis. Am. J. Physiol. 277, R434–R440. https://doi.org/10.1152/ajpregu.1999.277.2.R434.

11. Tiao, G., Lieberman, M., Fischer, J.E., and Hasselgren, P.O. (1997). Intracellular regulation of protein degradation during sepsis is different in fast- and slow-twitch muscle. Am. J. Physiol. 272, R849–R856. https://doi.org/10.1152/ajpregu.1997.272.3.R849.

12. Hobler, S.C., Tiao, G., Fischer, J.E., Monaco, J., and Hasselgren, P.O. (1998). Sepsis-induced increase in muscle proteolysis is blocked by specific proteasome inhibitors. Am. J. Physiol. 274, R30–R37. https://doi.org/10.1152/ajpregu.1998.274.1.R30.

13. Stana, F., Vujovic, M., Mayaki, D., Leduc-Gaudet, J.P., Leblanc, P., Huck, L., and Hussain, S.N.A. (2017). Differential Regulation of the Autophagy and Proteasome Pathways in Skeletal Muscles in Sepsis. Crit. Care Med. 45, e971–e979. https://doi.org/10.1097/CCM.0000000000002520.

14. Chai, J., Wu, Y., and Sheng, Z.Z. (2003). Role of ubiquitin-proteasome pathway in skeletal muscle wasting in rats with endotoxemia. Crit. Care Med. 31, 1802–1807. https://doi.org/10.1097/01.CCM.0000069728.49939.E4.

15. Callahan, L.A., and Supinski, G.S. (2009). Sepsis-induced myopathy. Crit. Care Med. 37, S354–S367. https://doi.org/10.1097/CCM.0b013e3181b6e439.

16. Morel, J., Palao, J.C., Castells, J., Desgeorges, M., Busso, T., Molliex, S., Jahnke, V., Del Carmine, P., Gondin, J., Arnould, D., et al. (2017). Regulation of Akt-mTOR, ubiquitin-proteasome and autophagy-lysosome pathways in locomotor and respiratory muscles during experimental sepsis in mice. Sci. Rep. 7, 10866. https://doi.org/10.1038/s41598-017-11440-5.

17. Parzych, K.R., and Klionsky, D.J. (2014). An overview of autophagy: morphology, mechanism, and regulation. Antioxid. Redox Signal. 20, 460–473. https://doi.org/10.1089/ars.2013.5371.

18. Mammucari, C., Milan, G., Romanello, V., Masiero, E., Rudolf, R., Del Piccolo, P., Burden, S.J., Di Lisi, R., Sandri, C., Zhao, J., et al. (2007). FoxO3 controls autophagy in skeletal muscle in vivo. Cell Metab. 6, 458–471. https://doi.org/10.1016/j.cmet.2007.11.001.

19. Doyle, A., Zhang, G., Abdel Fattah, E.A., Eissa, N.T., and Li, Y.P. (2011). Toll-like receptor 4 mediates lipopolysaccharide-induced muscle catabolism via coordinate activation of ubiquitin-proteasome and autophagy-lysosome pathways. FASEB J 25, 99–110. https://doi.org/10.1096/fj.10-164152.

20. Jamart, C., Gomes, A.V., Dewey, S., Deldicque, L., Raymackers, J.M., and Francaux, M. (2014). Regulation of ubiquitin-proteasome and autophagy pathways after acute LPS and epoxomicin administration in mice. BMC Musculoskelet. Disord. 15, 166. https://doi.org/10.1186/1471-2474-15-166.

21. Maes, K., Stamiris, A., Thomas, D., Cielen, N., Smuder, A., Powers, S.K., Leite, F.S., Hermans, G., Decramer, M., Hussain, S.N., and Gayan-Ramirez, G. (2014). Effects of controlled mechanical ventilation on sepsis-induced diaphragm dysfunction in rats. Crit. Care Med. 42, e772–e782. https://doi.org/10.1097/CCM.0000000000000685.

22. Mofarrahi, M., Sigala, I., Guo, Y., Godin, R., Davis, E.C., Petrof, B., Sandri, M., Burelle, Y., and Hussain, S.N.A. (2012). Autophagy and skeletal muscles in sepsis. PLoS One 7, e47265. https://doi.org/10.1371/journal.pone.0047265.

23. Leduc-Gaudet, J.P., Franco-Romero, A., Cefis, M., Moamer, A., Broering, F.E., Milan, G., Sartori, R., Chaffer, T.J., Dulac, M., Marcangeli, V., et al. (2023). MYTHO is a novel

regulator of skeletal muscle autophagy and integrity. Nat. Commun. 14, 1199. https://doi.org/10.1038/s41467-023-36817-1.

24. Zhao, J., Brault, J.J., Schild, A., Cao, P., Sandri, M., Schiaffino, S., Lecker, S.H., and Goldberg, A.L. (2007). FoxO3 coordinately activates protein degradation by the autophagic/lysosomal and proteasomal pathways in atrophying muscle cells. Cell Metab. 6, 472–483. https://doi.org/10.1016/j.cmet.2007.11.004.

25. Smuder, A.J., Sollanek, K.J., Nelson, W.B., Min, K., Talbert, E.E., Kavazis, A.N., Hudson, M.B., Sandri, M., Szeto, H.H., and Powers, S.K. (2018). Crosstalk between autophagy and oxidative stress regulates proteolysis in the diaphragm during mechanical ventilation. Free Radic. Biol. Med. 115, 179–190. https://doi.org/10.1016/j.freeradbiomed.2017.11.025.

26. Sandri, M. (2010). Autophagy in skeletal muscle. FEBS Lett. 584, 1411–1416. https://doi.org/10.1016/j.febslet.2010.01.056.

27. Masiero, E., Agatea, L., Mammucari, C., Blaauw, B., Loro, E., Komatsu, M., Metzger, D., Reggiani, C., Schiaffino, S., and Sandri, M. (2009). Autophagy is required to maintain muscle mass. Cell Metab. 10, 507–515.

28. Leduc-Gaudet, J.-P., Mayaki, D., Reynaud, O., Broering, F.E., Chaffer, T.J., Hussain, S.N.A., and Gouspillou, G. (2020). Parkin Overexpression Attenuates Sepsis-Induced Muscle Wasting. Cells 9, 1454.

29. Haspel, J., Shaik, R.S., Ifedigbo, E., Nakahira, K., Dolinay, T., Englert, J.A., and Choi, A.M.K. (2011). Characterization of macroautophagic flux in vivo using a leupeptin-based assay. Autophagy 7, 629–642. https://doi.org/10.4161/auto.7.6.15100.

30. Carnio, S., LoVerso, F., Baraibar, M.A., Longa, E., Khan, M.M., Maffei, M., Reischl, M., Canepari, M., Loefler, S., Kern, H., et al. (2014). Autophagy impairment in muscle induces neuromuscular junction degeneration and precocious aging. Cell Rep. 8, 1509–1521. https://doi.org/10.1016/j.celrep.2014.07.061.

31. Wu, J.J., Quijano, C., Chen, E., Liu, H., Cao, L., Fergusson, M.M., Rovira, I.I., Gutkind, S., Daniels, M.P., Komatsu, M., and Finkel, T. (2009). Mitochondrial dysfunction and oxidative stress mediate the physiological impairment induced by the disruption of autophagy. Aging (Albany NY) 1, 425–437. https://doi.org/10.18632/aging.100038.

32. Kim, K.H., Jeong, Y.T., Oh, H., Kim, S.H., Cho, J.M., Kim, Y.N., Kim, S.S., Kim, D.H., Hur, K.Y., Kim, H.K., et al. (2013). Autophagy deficiency leads to protection from obesity and insulin resistance by inducing Fgf21 as a mitokine. Nat. Med. 19, 83–92. https://doi.org/10.1038/nm.3014.

33. Lim, J.A., Zare, H., Puertollano, R., and Raben, N. (2017). Atg5(flox)-Derived Autophagy-Deficient Model of Pompe Disease: Does It Tell the Whole Story? Molecular therapy. Mol. Ther. Methods Clin. Dev. 7, 11–14. https://doi.org/10.1016/j.omtm.2017.08.002.

34. Schmidt, E.K., Clavarino, G., Ceppi, M., and Pierre, P. (2009). SUnSET, a nonradioactive method to monitor protein synthesis. Nat. Methods 6, 275–277. https://doi.org/10.1038/nmeth.1314.

35. Sandri, M., Sandri, C., Gilbert, A., Skurk, C., Calabria, E., Picard, A., Walsh, K., Schiaffino, S., Lecker, S.H., and Goldberg, A.L. (2004). Foxo transcription factors induce the atrophy-related ubiquitin ligase atrogin-1 and cause skeletal muscle atrophy. Cell 117, 399–412.

36. Pittet, D., Thiévent, B., Wenzel, R.P., Li, N., Auckenthaler, R., and Suter, P.M. (1996). Bedside prediction of mortality from bacteremic sepsis. A dynamic analysis of ICU patients. Am. J. Respir. Crit. Care Med. 153, 684–693. https://doi.org/10.1164/ajrccm.153.2.8564118.

37. Cauvi, D.M., Song, D., Vazquez, D.E., Hawisher, D., Bermudez, J.A., Williams, M.R., Bickler, S., Coimbra, R., and De Maio, A. (2012). Period of irreversible therapeutic intervention during sepsis correlates with phase of innate immune dysfunction. J. Biol. Chem. 287, 19804–19815. https://doi.org/10.1074/jbc.M112.359562.

38. Nemzek, J.A., Xiao, H.Y., Minard, A.E., Bolgos, G.L., and Remick, D.G. (2004). Humane endpoints in shock research. Shock 21, 17–25. https://doi.org/10.1097/01.shk.0000101667.49265.fd.

39. Block, B.A. (1994). Thermogenesis in muscle. Annu. Rev. Physiol. 56, 535–577. https://doi.org/10.1146/annurev.ph.56.030194.002535.

40. Rowland, L.A., Bal, N.C., and Periasamy, M. (2015). The role of skeletal-muscle-based thermogenic mechanisms in vertebrate endothermy. Biol. Rev. Camb. Philos. Soc. 90, 1279–1297. https://doi.org/10.1111/brv.12157.

41. Karsli-Uzunbas, G., Guo, J.Y., Price, S., Teng, X., Laddha, S.V., Khor, S., Kalaany, N.Y., Jacks, T., Chan, C.S., Rabinowitz, J.D., and White, E. (2014). Autophagy is required for glucose homeostasis and lung tumor maintenance. Cancer Discov. 4, 914–927.

42. Gomes, M.D., Lecker, S.H., Jagoe, R.T., Navon, A., and Goldberg, A.L. (2001). Atrogin-1, a muscle-specific F-box protein highly expressed during muscle atrophy. Proc. Natl. Acad. Sci. USA. 98, 14440–14445. https://doi.org/10.1073/pnas.251541198.

43. Bodine, S.C., Latres, E., Baumhueter, S., Lai, V.K., Nunez, L., Clarke, B.A., Poueymirou, W.T., Panaro, F.J., Na, E., Dharmarajan, K., et al. (2001). Identification of ubiquitin ligases required for skeletal muscle atrophy. Science 294, 1704–1708. https://doi.org/10.1126/science.1065874.

44. Sartori, R., Schirwis, E., Blaauw, B., Bortolanza, S., Zhao, J., Enzo, E., Stantzou, A., Mouisel, E., Toniolo, L., Ferry, A., et al. (2013). BMP signaling controls muscle mass. Nat. Genet. 45, 1309–1318. https://doi.org/10.1038/ng.2772.

45. Milan, G., Romanello, V., Pescatore, F., Armani, A., Paik, J.-H., Frasson, L., Seydel, A.,

Zhao, J., Abraham, R., Goldberg, A.L., et al. (2015). Regulation of autophagy and the ubiquitin–proteasome system by the FoxO transcriptional network during muscle atrophy. Nat. Commun. 6, 6670. https://doi.org/10.1038/ncomms7670.

46. Lo Verso, F., Carnio, S., Vainshtein, A., and Sandri, M. (2014). Autophagy is not required to sustain exercise and PRKAA1/AMPK activity but is important to prevent mitochondrial damage during physical activity. Autophagy 10, 1883–1894. https://doi.org/10.4161/auto.32154.

47. Rooyackers, O.E., Kersten, A.H., and Wagenmakers, A.J. (1996). Mitochondrial protein content and in vivo synthesis rates in skeletal muscle from critically ill rats. Clin. Sci. 91, 475–481.

48. Callahan, L.A., and Supinski, G.S. (2005). Sepsis induces diaphragm electron transport chain dysfunction and protein depletion. Am. J. Respir. Crit. Care Med. 172, 861–868. https://doi.org/10.1164/rccm.200410-1344OC.

49. Crouser, E.D., Julian, M.W., Blaho, D.V., and Pfeiffer, D.R. (2002). Endotoxin-induced mitochondrial damage correlates with impaired respiratory activity. Crit. Care Med. 30, 276–284.

50. Protti, A., Carré, J., Frost, M.T., Taylor, V., Stidwill, R., Rudiger, A., and Singer, M. (2007). Succinate recovers mitochondrial oxygen consumption in septic rat skeletal muscle. Crit. Care Med. 35, 2150–2155.

51. Crowell, K.T., Soybel, D.I., and Lang, C.H. (2017). Restorative Mechanisms Regulating Protein Balance in Skeletal Muscle During Recovery From Sepsis. Shock 47, 463–473. https://doi.org/10.1097/SHK.0000000000000762.

52. Cahill, G.F. (2006). Fuel Metabolism in Starvation. Annu. Rev. Nutr. 26, 1–22.

53. Zhou, C., and Byard, R.W. (2017). Septic Ketoacidosis-A Potentially Lethal Entity with Renal Tubular Epithelial Vacuolization. J. Forensic Sci. 62, 122–125. https://doi.org/10.1111/1556-4029.13245.

54. Ezaki, J., Matsumoto, N., Takeda-Ezaki, M., Komatsu, M., Takahashi, K., Hiraoka, Y., Taka, H., Fujimura, T., Takehana, K., Yoshida, M., et al. (2011). Liver autophagy contributes to the maintenance of blood glucose and amino acid levels. Autophagy 7, 727–736. https://doi.org/10.4161/auto.7.7.15371.

55. Oami, T., Watanabe, E., Hatano, M., Teratake, Y., Fujimura, L., Sakamoto, A., Ito, C., Toshimori, K., Swanson, P.E., and Oda, S. (2018). Blocking Liver Autophagy Accelerates Apoptosis and Mitochondrial Injury in Hepatocytes and Reduces Time to Mortality in a Murine Sepsis Model. Shock 50, 427–434. https://doi.org/10.1097/SHK.0000000000001040.

56. Thiessen, S.E., Derese, I., Derde, S., Dufour, T., Pauwels, L., Bekhuis, I., Pintelon, I., Martinet, W., Van den Berghe, G., and Vanhorebeek, I. (2017). The Role of Autophagy in Critical Illness-induced Liver

Damage. Sci. Rep. 7, 14150. https://doi.org/10.1038/s41598-017-14405-w.

57. Oami, T., Watanabe, E., Hatano, M., Sunahara, S., Fujimura, L., Sakamoto, A., Ito, C., Toshimori, K., and Oda, S. (2017). Suppression of T Cell Autophagy Results in Decreased Viability and Function of T Cells Through Accelerated Apoptosis in a Murine Sepsis Model. Crit. Care Med. 45, e77–e85. https://doi.org/10.1097/CCM.0000000000002016.

58. Gouspillou, G., Sgarioto, N., Norris, B., Barbat-Artigas, S., Aubertin-Leheudre, M., Morais, J.A., Burelle, Y., Taivassalo, T., and Hepple, R.T. (2014). The relationship between muscle fiber type-specific PGC-1alpha content and mitochondrial content varies between rodent models and humans. PLoS One 9, e103044. https://doi.org/10.1371/journal.pone.0103044.

59. Schiaffino, S., and Reggiani, C. (2011). Fiber types in mammalian skeletal muscles. Physiol. Rev. 91, 1447–1531. https://doi.org/10.1152/physrev.00031.2010.

60. Hall, M.J., Williams, S.N., DeFrances, C.J., and Golosinskiy, A. (2011). Inpatient care for septicemia or sepsis: a challenge for patients and hospitals. NCHS Data Brief, 1–8.

61. Komatsu, M., Waguri, S., Ueno, T., Iwata, J., Murata, S., Tanida, I., Ezaki, J., Mizushima, N., Ohsumi, Y., Uchiyama, Y., et al. (2005). Impairment of starvation-induced and constitutive autophagy in Atg7-deficient mice. J. Cell Biol. 169, 425–434. https://doi.org/10.1083/jcb.200412022.

62. Schuler, M., Ali, F., Metzger, E., Chambon, P., and Metzger, D. (2005). Temporally controlled targeted somatic mutagenesis in skeletal muscles of the mouse. Genesis 41, 165–170. https://doi.org/10.1002/gene.20107.

63. Kiermayer, C., Conrad, M., Schneider, M., Schmidt, J., and Brielmeier, M. (2007). Optimization of spatiotemporal gene inactivation in mouse heart by oral application of tamoxifen citrate. Genesis 45, 11–16. https://doi.org/10.1002/dvg.20244.

64. Robinson, S.P., Langan-Fahey, S.M., Johnson, D.A., and Jordan, V.C. (1991). Metabolites, pharmacodynamics, and pharmacokinetics of tamoxifen in rats and mice compared to the breast cancer patient. Drug Metab. Dispos. 19, 36–43.

65. Buras, J.A., Holzmann, B., and Sitkovsky, M. (2005). Animal models of sepsis: setting the stage. Nat. Rev. Drug Discov. 4, 854–865. https://doi.org/10.1038/nrd1854.

66. Ruiz, S., Vardon-Bounes, F., Merlet-Dupuy, V., Conil, J.-M., Buléon, M., Fourcade, O., Tack, I., and Minville, V. (2016). Sepsis modeling in mice: ligation length is a major severity factor in cecal ligation and puncture. Intensive Care Med. Exp. 4, 22.

67. Toscano, M.G., Ganea, D., and Gamero, A.M. (2011). Cecal ligation puncture procedure. J. Vis. Exp. https://doi.org/10.3791/2860.

68. Gonnert, F.A., Recknagel, P., Seidel, M., Jbeily, N., Dahlke, K., Bockmeyer, C.L., Winning, J., Lösche, W., Claus, R.A., and Bauer, M. (2011). Characteristics of clinical sepsis reflected in a reliable and reproducible rodent sepsis model. J. Surg. Res. 170, e123–e134. https://doi.org/10.1016/j.jss.2011.05.019.

69. Leduc-Gaudet, J.-P., Reynaud, O., Hussain, S.N., and Gouspillou, G. (2019). Parkin overexpression protects from ageing-related loss of muscle mass and strength. J. Physiol. 597, 1975–1991. https://doi.org/10.1113/JP277157.

70. Mofarrahi, M., McClung, J.M., Kontos, C.D., Davis, E.C., Tappuni, B., Moroz, N., Pickett, A.E., Huck, L., Harel, S., Danialou, G., and Hussain, S.N.A. (2015). Angiopoietin-1 enhances skeletal muscle regeneration in mice. Am. J. Physiol. Regul. Integr. Comp. Physiol. 308, R576–R589. https://doi.org/10.1152/ajpregu.00267.2014.

71. Gouspillou, G., Godin, R., Piquereau, J., Picard, M., Mofarrahi, M., Mathew, J., Purves-Smith, F.M., Sgarioto, N., Hepple, R.T., Burelle, Y., and Hussain, S.N.A. (2018). Protective role of Parkin in skeletal muscle contractile and mitochondrial function. J. Physiol. 596, 2565–2579. https://doi.org/10.1113/JP275604.

72. Gouspillou, G. (2023). MitoFun: Code to Analyze Mitochondrial Respiration, H2O2 Emission and Calcium Retention Capacity Data in Igor Pro (Wavemetrics).

73. Leduc-Gaudet, J.P., Picard, M., St-Jean Pelletier, F., Sgarioto, N., Auger, M.J., Vallée, J., Robitaille, R., St-Pierre, D.H., and Gouspillou, G. (2015). Mitochondrial morphology is altered in atrophied skeletal muscle of aged mice. Oncotarget 6, 17923–17937. https://doi.org/10.18632/oncotarget.4235.

74. Briguet, A., Courdier-Fruh, I., Foster, M., Meier, T., and Magyar, J.P. (2004). Histological parameters for the quantitative assessment of muscular dystrophy in the mdx-mouse. Neuromuscul. Disord. 14, 675–682. https://doi.org/10.1016/j.nmd.2004.06.008.

75. Dulac, M., Leduc-Gaudet, J.P., Reynaud, O., Ayoub, M.B., Guérin, A., Finkelchtein, M., Hussain, S.N., and Gouspillou, G. (2020). Drp1 knockdown induces severe muscle atrophy and remodelling, mitochondrial dysfunction, autophagy impairment and denervation. J. Physiol. 598, 3691–3710. https://doi.org/10.1113/JP279802.

76. Ritchie, M.E., Phipson, B., Wu, D., Hu, Y., Law, C.W., Shi, W., and Smyth, G.K. (2015). limma powers differential expression analyses for RNA-sequencing and microarray studies. Nucleic Acids Res. 43, e47. https://doi.org/10.1093/nar/gkv007.

STAR★METHODS

KEY RESOURCES TABLE

REAGENT or RESOURCE	SOURCE	IDENTIFIER
Antibodies (Immunoblot)		
Atg7 (D12B11)	Cell Signaling Technology	Cat# #8558; RRID:AB_10831194
LC3A/B (D3U4C) XP®	Cell Signaling Technology	Cat# 12741; RRID:AB_2617131
rabbit anti-GAPDH	Cell Signaling Technology	Cat# 2118; RRID:AB_561053
Phospho-FoxO1 (Ser256)	Cell Signaling Technology	Cat# 9461; RRID:AB_329831
FoxO1 (L27)	Cell Signaling Technology	Cat# 9454; RRID:AB_823503
Phospho-FoxO3a (Ser253)	Cell Signaling Technology	Cat# 9466; RRID:AB_2106674
FoxO3a (75D8)	Cell Signaling Technology	Cat# 2497; RRID:AB_836876
BNIP3	Sigma-Aldrich	Cat# B7931; RRID:AB_258637
p62/SQSTM1	Novus Biologicals Inc.	Cat# H00008878-M01; RRID:AB_548364
Anti-puromycin, clone 12D10	Millipore	Cat# MABE343; RRID:AB_2566826
Total OXPHOS	Abcam	Cat# ab110413; RRID:AB_2629281
Mono- and polyubiquitinylated conjugates mAb (FK2)	Enzo Life Sciences	Cat# BML-PW8810; RRID:AB_10541840
Rabbit Anti-Mouse IgG - H&L	Abcam	Cat# ab6728; RRID:AB_955440
Goat Anti-Rabbit IgG - H&L	Abcam	Cat# ab6721; RRID:AB_955447
Antibodies (immunofluorescence)		
Anti-Laminin	Sigma-Aldrich	Cat# L9393; RRID:AB_477163
mouse IgG2b monoclonal anti-MHC type I	DSHB	Cat# BA-F8; RRID:AB_10572253
mouse IgG1 monoclonal anti-MHC type IIa	DSHB	Cat# SC-71; RRID:AB_2147165
mouse IgM monoclonal anti-MHC type IIb	DSHB	Cat# BF-F3; RRID:AB_2266724
p62/SQSTM1	Novus Biologicals Inc.	Cat# H00008878-M01; RRID:AB_548364
Alexa Fluor 350 IgG2b goat anti-mouse	Thermo Fisher Scientific	Cat# A-21140; RRID:AB_2535777
Alexa Fluor 488 IgG goat anti-rabbit	Thermo Fisher Scientific	Cat# A-11008; RRID:AB_143165
Alexa Fluor 488 IgM goat anti-mouse	Thermo Fisher Scientific	Cat# A-21042; RRID:AB_2535711
Alexa Fluor 488 IgG2a goat anti-mouse	Thermo Fisher Scientific	Cat# A-21131; RRID:AB_2535771
Alexa Fluor 594 IgG1 (y1) goat anti-mouse	Thermo Fisher Scientific	Cat# A-21125; RRID:AB_2535767
Alexa Fluor 594 IgG goat anti-rabbit	Thermo Fisher Scientific	Cat# A-11037; RRID:AB_2534095
Alexa Fluor 568 IgG goat anti-rabbit	Thermo Fisher Scientific	Cat# A-11011; RRID:AB_143157
Biological samples		
Mouse skeletal muscles	This paper	N/A
Chemicals, peptides, and recombinant proteins		
Leupeptin	Sigma-Aldrich	Cat#L2884, CAS: 103476-89-7
Puromycin	Sigma-Aldrich	Cat#P8833, CAS: 58-58-2
TRIzol™ Reagent	Invitrogen™	Cat#15596026
Lactobionic acid	Sigma-Aldrich	Cat#61321, CAS: 96-82-2
Laemmli	Boston Bioproducts Inc	Cat#BP-111R
L-(−)-Malic acid	MilliporeSigma	M1000, CAS: 97-67-6
Oligomycin	MilliporeSigma	O4876; CAS: 1404-19-9
Adenosine 5'-diphosphate monopotassium salt dihydrate	MilliporeSigma	A5285, CAS: 72696-48-1
Glutaraldehyde solution	MilliporeSigma	G5882, CAS: 111-30-8

(Continued on next page)

20   iScience 26, 107475, August 18, 2023

Continued

REAGENT or RESOURCE	SOURCE	IDENTIFIER
Adenosine 5'-triphosphate disodium salt	MilliporeSigma	A2383, CAS: 34369-07-8
Bovine Serum Albumin	MilliporeSigma	A8806, CAS: 9048-46-8
Hydrogen peroxide	MilliporeSigma	95321, CAS: 7722-84-1
2-Methylbutane	MilliporeSigma	M32631, CAS: 78-78-4
Tragacanth	MilliporeSigma	G1128, CAS: 9000-65-1
Saponin	MilliporeSigma	S7900, CAS: 8047-15-2
Sodium azide	Sigma-Aldrich	S2002, CAS: 26628-22-8
Sodium cacodylate trihydrate	MilliporeSigma	C4945, CAS: 6131-99-3
Taurine	MilliporeSigma	T0625, CAS: 107-35-7
Dipotassium phosphate (K_2HPO_4)	MilliporeSigma	P3786, CAS: 7758-11-4
Goat Serum	Thermo Fisher Scientific	Cat# 50062Z
Triton X-100	Sigma-Aldrich	Cat# X100-500ML, CAS: 9002-93-1
Tween 20	Thermo Fisher Scientific	Cat# 85113, CAS:9005-64-5
O.C.T. compound	Fisher Scientific	Cat# 12351753
Prolong™ Gold	Invitrogen™	Cat# P36930
Calcium Green™-5N, Hexapotassium Salt	Invitrogen™	Cat# C3737
Fisherbrand™ Superfrost™ Plus Microscope Slides	Fisher Scientific	Cat# 22-037-246
Ponceau	MilliporeSigma	P3504, CAS: 6226-79-5
Power SYBR™ Green PCR Master Mix	Applied Biosystems™	Cat# 4368702
OmniPur® EGTA	MilliporeSigma	4100-OP, CAS: 67-42-5
Critical commercial assays		
PureLink™ RNA Mini Kit	Invitrogen™	Cat# 12183018A
SuperScript™ IV Reverse Transcriptase	Invitrogen™	Cat# 18090050
Deposited data		
Microarray data	NCBI Gene Expression Omnibus (GEO) database	Accession number: GSE234838
Experimental models: Organisms/strains		
Mouse: C57BL6/N wild type	Charles River Laboratories	N/A
Mouse: HSA-Cre-ERT2	(Schuler, Ali et al.[62])	N/A
Mouse: Atg7fl/fl	(Komatsu, Waguri et al.[61])	N/A
Oligonucleotides		
Primers for RT-qPCR, see Table S2	This paper	N/A
Software and algorithms		
GraphPad Prism 8 software	GraphPad	https://www.graphpad.com/ RRID: SCR_002798
ImageJ (for image analysis)	NIH	https://imagej.nih.gov/ij/ RRID:SCR_003070
Igor Pro	WaveMetrics	RRID:SCR_000325
MitoFun	(Gouspillou[72])	https://doi.org/10.5281/zenodo.7510439
Transcriptome Analysis Console Software	Affymetrix	Version 4.0; RRID:SCR_018718
ImageLab	Bio-Rad Laboratories	Versions 5.1 and 6.1
BioRender	BioRender	https://biorender.com/ RRID:SCR_018361
TSE PhenoMaster software	TSE systems	https://www.tse-systems.com/

Continued

REAGENT or RESOURCE	SOURCE	IDENTIFIER
R package for Microarray Data (Limma)	(Ritchie, Phipson et al.[76])	https://www.bioconductor.org/packages/release/bioc/html/limma.html
Dynamic Muscle Control and Analysis Software	Aurora Scientific	N/A
DatLab Software	Oroboros Instruments	https://www.oroboros.at/index.php/product/datlab/
Other		
Chow diet	Envigo	Teklad global 18% protein irradiated rodent diet 2918
Mini-PROTEAN™ TGX Stain-Free™ Protein Gels	Bio-Rad	Cat#4568086
Trans-Blot (R)Turbo, Midi Format, 0.2mm PVDF	Bio-Rad	Cat# 1704157
Tamoxifen diet	Teklad	
BIO-GS3 Grip Strength Test	BIOSEB	www.bioseb.com
AutoClip® System	Fine Science Tools	No. 12020-09 100
Wound clips, 9mm	Fine Science Tools	No. 12022-09
Freestyle Optium Neo ketometer	Abbott	N/A
Accu-Chek handheld glucometer	Roche Diagnostics	N/A
Isoflurane	Piramal Critical Care, Inc.	N/A
3-0 absorbable polyfilament suture	Johnson & Johnson	N/A
EchoMRI	EchoMRI™	RRID:SCR_017104
Thermalert TH-5 thermometer	Physitemp Instruments, Inc.	N/A

RESOURCE AVAILABILITY

Lead contact

Further information and requests for resources and reagents should be directed to and will be fulfilled by the lead contact, Gilles Gouspillou (gouspillou.gilles@uqam.ca).

Materials availability

This study did not generate new unique reagents.

Data and code availability

- All data reported in this paper will be shared by the lead contact upon request.

- Microarray data generated in this study have been deposited at GEO and are publicly available as of the date of publication. Accession number is listed in the key resources table. Microscopy and western blot data reported in this paper will be shared by the lead contact upon request.

- The code developed to analyze mitochondrial function data in the Igor Pro 8 software (MitoFun) has been deposited at Zenodo and is publicly available as of the date of publication. DOI is listed in the key resources table:

EXPERIMENTAL MODEL AND STUDY PARTICIPANT DETAILS

All mice used in this study originated from a C57BL6/J genetic background. Atg7 floxed mice[61] were crossed with mice expressing Cre-ER^T2 driven by human skeletal Actin (HSA) promoter.[62] Resultant HSA-Cre-ER^T2 Atg7^f/f mice were fed *ad libitum* with a certified rodent diet containing tamoxifen citrate (400 mg/kg) (Teklad TAM400/CreER, Envigo, Madison, WI) for 10 weeks,[63] then returned to a standard chow diet (Teklad global 18% protein irradiated rodent diet 2918, Envigo) for 2-3 weeks to ensure elimination of tamoxifen from the serum prior to surgery.[64] Mice fed this diet (Atg7^iSkM-KO) were compared to sex and age-matched HSA-Cre-ER^T2 Atg7^f/f mice that were fed a standard chow diet only. To control for the effects of tamoxifen diet *per se*, C57BL/6J mice (Charles River Laboratories, Saint-Constant, QC, Canada) fed according to the same tamoxifen protocol as described above were used as additional controls (Figure S1). All mice were group housed under a standard 12:12 h light/dark cycle at 22°C. All experiments

involving animals were approved by the Research Ethics Board of the Research Institute of the McGill University Health Center (MUHC-RI; #2014-7549) and were performed in accordance with the principles outlined by the Canadian Council of Animal Care. The sex of mice used in each experiment is provided in the Results section, in the Figures and/or in the Figure legends.

METHOD DETAILS

Cecal ligation and puncture

Cecal ligation and puncture (CLP) was performed to induce polymicrobial sepsis, as described previously,[13] with minor modifications. The CLP model is known to accurately mimic the clinical features of human sepsis.[65] Briefly, mice were anesthetized using ~3% isoflurane with air (Piramal Critical Care, Bethlehem, PA) and a midline abdominal incision (~2 cm) was performed. The caecum was carefully ligated at ~1 cm from its distal end to control for the degree of disease severity[66,67] then perforated via a through-and-through puncture with a 25.5 gauge needle in a sterile environment, leaving 2 holes. The ligated caecum was gently compressed to extrude a small amount of cecal contents through the punctured holes, then replaced in the abdominal cavity. The peritoneum was closed in two separate layers using 3-0 absorbable polyfilament interrupted sutures and the skin was closed with a 9 mm surgical staple (AutoClip® System, Fine Science Tools, Foster City, CA). All animals received subcutaneous injections of Buprenex® (0.05 to 0.2 mg/kg buprenorphine in 1 ml of 0.9% saline) immediately after surgery and every 12 h thereafter to minimize pain (0.05 mg/kg in ~100 μL of 0.9% saline). Sham-operated mice were subjected to identical procedures, except for cecal ligation and puncture. Age- and gender-matched controls were included for all procedures. Animals were returned to their cages (3-5 mice per cage) with free access to food and water, unless stated otherwise. All animals were closely monitored by animal care staff blinded to surgical status and genotype for signs of excessive pain or distress, such as lack of movement agonized breathing, or excessive body mass loss (20%). Any mouse determined to be moribund was euthanized. Several mice were sacrificed 48 h post-surgery for use in muscle contractility and mitochondrial function tests. Mice that were used for 6-day measurements were monitored more intensively, at least 3-5 times daily. To minimize suffering, temperature was measured daily using a rectal probe. If body temperature dropped more than 4°C, animals were euthanized. A daily clinical severity score (CSS) was assigned to track the course of the disease and to minimize excessive pain or distress, as previously described.[68] Grade 1 was interpreted as no signs of illness, grade 2 as mild signs (e.g., less active, slightly hunched posture), grade 3 as medium severe signs (e.g., less active, hunched, and slow movement), and grade 4 as very severe signs (e.g., lethargic, severely hunched, no movement, agonal breathing, and moribund). Mice were euthanized with CO_2 and death was confirmed by cervical dislocation.

In situ measurement of TA contractility

To determine skeletal muscle contractile function, animals were anesthetized with an intraperitoneal injection of a ketamine-xylazine cocktail (ketamine: 130 mg/kg; xylazine: 20 mg/kg). Anesthesia was maintained with 0.05 mLl supplemental doses, as needed. A Dynamic Muscle Control and Analysis Software (DMC/DMA) Suite was used for collection and data analysis (Aurora Scientific, Aurora, ON). The distal tendon of the left TA muscle was isolated and attached to the arm of a 305C-LR dual-mode muscle lever with 4.0 surgical silk, as previously described, with minor modifications.[69–71] The partially exposed muscle surface was kept moist and directly stimulated with an electrode placed on the belly of the muscle. Optimal muscle length and voltage was progressively adjusted to produce maximal tension and length was measured with a microcaliper. The pulse duration was set to 0.2 ms for all tetanic contractions. Force-frequency relationship curves were determined at muscle optimal length at 10, 30, 50, 70, 100, 120, 150 and 200Hz, with 1 min intervals between stimulations to avoid fatigue. Following tetanic-force measurements, the muscle was rested for 2 min then subjected to a fatigue resistance protocol of 60 tetanic contractions (75 Hz/200 ms) every 2 s for a total of 2 min. At the end of each experiment, mice were sacrificed, and muscles were carefully dissected, weighed, and frozen in liquid nitrogen or in isopentane pre-cooled in liquid nitrogen. *In situ* muscle force was normalized to tissue cross-sectional area (expressed as Newtons/cm^2). Muscle cross-sectional area was estimated by dividing muscle mass by the product of muscle length and muscle density (1.056 g/cm^3).

Preparation of permeabilized muscle fibers

Mitochondrial function was determined in freshly excised GAS muscles at 2-day post-surgery. Left GAS muscles were rapidly dissected and immersed in ice-cold (4°C) stabilizing buffer A (2.77 mM CaK2

EGTA, 7.23 mM K2 EGTA, 6.56 mM MgCl2, 0.5 mM dithiothreitol (DTT), 50 mM 2-(N-morpholino) ethane-sulfonic acid potassium salt (K-MES), 20 mM imidazol, 20 mM taurine, 5.3 mM Na2 ATP, and 15 mM phosphocreatine, pH 7.3). Different regions of the GAS muscle have different muscle fiber type composition and the following protocol was used to minimize variance in results. Mitochondrial respiration and H_2O_2 emission were performed in the oxidative red GAS while the assessment of the mitochondrial permeability transition pore sensitivity to Ca^{2+} was assessed in the glycolytic white GAS. GAS samples were weighed then separated into small fiber bundles using fine forceps and a Leica S4 E surgical dissecting microscope (Leica Microsystems, Wetzlar, Germany). Muscle fiber bundles were incubated for 30 min at low rocking speed in glass scintillation vials containing buffer A supplemented with 0.05 mg/mL saponin to selectively permeabilize the sarcolemma. Red fiber bundles used for respiration and H_2O_2 emission analyses were then washed 3 times for 10 min at low rocking speed in buffer Z (110 mM, 35 mM KCl, 1 mM EGTA, 3 mM $MgCl_2$, and 10 mM K_2HPO_4, pH 7.3) at 4°C, supplemented with 5 mg/mL BSA. White fiber bundles used for CRC were washed 3 times for 10 min at low rocking speed in buffer C (80 mM K-MES, 50 mM HEPES, 20 mM taurine, 0.5 mM DTT, 10 mM $MgCl_2$, and 10 mM ATP, pH 7.3) at 4°C. Bundles were then transferred into buffer D (800 mM KCl, 50 mM HEPES, 20 mM taurine, 0.5 mM DTT, 10 mM $MgCl_2$, and 10 mM ATP, pH 7.3) for 30 min at 4°C. CRC bundles were then washed 3 times in a low-EGTA CRC buffer (250 mM sucrose, 10 mM Tris, 5 µM EGTA, and 10 mM 3-(*N-morpholino*) propane sulfonic acid (MOPS, pH 7.3) at 4°C and kept on ice until measurements were performed.

Mitochondrial respiration

Mitochondrial respiration was measured at 37°C in 2 mL of buffer Z using an Oxygraph O2K system (Oroboros Instruments, Innsbruck, AT). Briefly, 3 to 6 mg (wet mass) of GAS bundled fibers were weighed and added to the respiration chamber. The following substrates were added sequentially: 10 mM glutamate, 5 mM malate (G+M), and 2 mM ADP. Respiration rate was normalized as nanomoles per min per mg of wet muscle mass. All respiration experiments were analyzed with a MitoFun,[72] a homemade code to analyze mitochondrial function data in the Igor Pro 8 software (Wavemetrics, OR, USA).

Mitochondrial H_2O_2 production

H_2O_2 production was measured using an Amplex Red/horseradish peroxidase (HRP) assay, a Hitachi FL-2500 fluorescence spectrophotometer (excitation/emission wavelength of 563/587 nm), and FL Solutions software. Following a period of baseline autofluorescence, 4–6 mg (wet mass) of GAS bundled fibers were weighed and inserted into a thermojacketed, magnetically stirred cuvette containing 600 µL of buffer Z, Amplex Red (5.5 µM), and HRP (1 U/ml) at 37°C. The following substrates and inhibitors were added sequentially: glutamate (5 mM) and malate (5 mM), succinate (5 mM), ADP (0.1 mM), ADP (1 mM) and AA (400µM). H_2O_2 production was normalized as picomoles per min per mg of wet mass. All H_2O_2 emission experiments were analyzed with MitoFun,[72] a homemade code to analyze mitochondrial function data in the Igor Pro 8 software (Wavemetrics, OR, USA).

Mitochondrial Ca^{2+} retention capacity (CRC)

Sensitivity to mitochondrial permeability transition pore (mPTP) opening was evaluated by determining the CRC of mitochondria. GAS bundled fibers were placed in a cuvette with 600 µL of CRC assay mix (10 mM Pi, 2.5 mM malate, 5 mM glutamate, 0.5 nM oligomycin, 1 µM calcium green) at 37°C. Fluorescence was measured using a Hitachi F2500 spectrophotometer and FL Solutions software with excitation and emission detectors set at 505 and 535 nm and progressive uptake of Ca^{2+}. Ca^{2+} uptake and release were recorded over 5-10 min. The time to pore opening was analyzed as the total amount of Ca^{2+} intake by the mitochondria before Ca^{2+} release. All CRC experiments were analyzed with MitoFun,[72] a homemade code to analyze mitochondrial function data in the Igor Pro 8 software (Wavemetrics, OR, USA).

Transmission electron microscopy

Small strips prepared from GAS fibers were fixed in 2% glutaraldehyde buffer solution in 0.1 M cacodylate, pH 7.4, then post-fixed in 1% osmium tetroxide in 0.1 M cacodylate buffer. Tissues were dehydrated using a gradient of increasing concentrations of methanol to propylene oxide and infiltrated and embedded in EPON™ at the Facility for Electron Microscopy Research at McGill University. Ultrathin longitudinal sections (60 nm) were cut with a Reichert-Jung Ultracut III ultramicrotome (Leica Microsystems), mounted on nickel carbon-formvar coated grids, and stained with uranyl acetate and lead citrate. Sections were imaged using

a FEI Tecnai 12 transmission electron microscope at 120 kV and images were digitally captured using an AMT XR80C CCD camera system.

Measurement of myofiber atrophy

TA samples were mounted in tragacanth (Sigma-Aldrich # G1128) on plastic blocks and frozen in liquid iso-pentane cooled in liquid nitrogen and stored at -80°C. Samples were cut into 10μm cross-sections using a cryostat at -20°C then mounted on lysine coated slides (Superfrost), as described in.[69,73] Cross-sections were brought to room temperature, rehydrated with PBS (pH 7.2), then blocked with goat serum (10% in PBS). They were then incubated with primary polyclonal anti-laminin rabbit IgG antibody (Sigma-Aldrich # L9393, 1:500) for 1 h at room temperature. Sections were then washed three times in PBS before being incubated for 1 h at room temperature with an Alexa Fluor® 594 goat anti-rabbit IgG antibody (A-11037, 1:500). Sections were then washed three times in PBS and slides were cover slipped using Prolong™ Gold (P36930, Invitrogen) as a mounting medium. Slides were imaged with a Zeiss fluorescence microscope (Zeiss Axio Imager 2). Median distribution of minimum Feret diameters of at least 300 fibers per muscle sample were analyzed using ImageJ (NIH, Bethesda, MD).[74] The degree of myofiber atrophy was calculated as percent difference in mean minimum Feret diameters, relative to muscles of sham Atg7$^{f/f}$ mice. The means, fibers distributions, and average number of fibers analyzed per muscle per mouse are shown in Figure S6.

p62/SQSTM1 positive myofibers

Sections were stained to assess p62 positive fibers as previously described.[75] Muscle sections were first allowed to reach room temperature and rehydrated with PBS (pH 7.2) and then fixed in 4% PFA, permeabilized in 0.1% Triton X-100 in PBS for 15min. Slides were then washed three additional times with PBS and then blocked with goat serum (10% in PBS) for 1 hour. After, muscle sections were incubated for 1 hour at room temperature with anti-mouse p62/SQSTM1 (Novus Biologicals Inc. clone 2C11, 1:200). Sections were then washed three times in PBS before being incubated for 1 h at room temperature with an Alexa Fluor® 488 goat anti-mouse IgG antibody (A-21131, 1:500). Myofibers positive for p62 were quantified as a percentage of the total number of fibers counted.

Assessment of fiber type composition

TA muscle sections were immunolabeled for myosin heavy chain (MHC) types I, IIa and IIb, as previously described.[73] Cross-sections were brought to room temperature, rehydrated with PBS (pH 7.2), then blocked with goat serum (10% in PBS). They were then incubated for 1 h at room temperature with the following primary antibody cocktail: mouse IgG2b monoclonal anti-myosin heavy chain (MHC) type I (BA-F8, 1:25), mouse IgG1 monoclonal anti-MHC type IIa (SC-71,1:200), mouse IgM monoclonal anti-MHC type IIb (BF-F3, 1:200), and rabbit IgG polyclonal anti-Laminin (Sigma-Aldrich # L9393, 1:500). Sections were then washed three times in PBS before being incubated for 1 h at room temperature with the following Alexa Fluor® secondary antibody cocktail: Alexa Fluor® 350 goat anti-mouse IgG2b (y2b) (A-21140), Alexa Fluor® 594 goat anti-mouse IgG1 (y1) (A-21125, 1:500), Alexa Fluor® 488 goat anti-mouse IgM (A-21042,1:500), and Alexa Fluor® 488 goat anti-rabbit IgG (A-11008, 1:500). They were then washed three times in PBS and slides were cover slipped using Prolong™ Gold (P36930) as a mounting medium. Images were captured using a Zeiss Axio Imager M2. All MHC-targeting primary antibodies were purchased from the Developmental Studies Hybridoma Bank (DSHB) at the University of Iowa. Fiber type analyses were measured by a single observer blinded to sample identity.

Body composition analysis

Baseline (prior to surgery) body mass were recorded and thereafter at various timepoints post-surgery. The body mass loss for each animal was calculated as percent difference relative to baseline body mass. In a separate experiment, lean and fat mass were measured in live animals without anesthesia or sedation using an EchoMRI™, prior to surgery and 4 days post-surgery. Lean and fat mass loss for each animal was calculated as percent difference relative to baseline values.

Grip strength assessment

Forelimb grip strength was measured 3 days prior to surgery using a grip strength meter with a metal grid (Bioseb, Vitrolles, FR). Mice were held at the base of the tail then placed slightly above the grid to enable the animal to grab hold of it. They were then gently pulled away until the grid was released. Maximum force

in grams exerted by each mouse was recorded 3 times with a 3-minute interval between each measurement, to prevent fatigue. Data are expressed as average grams of force divided by body mass. All measurements were performed by an investigator blinded to mouse genotype.

Quantification of blood metabolites

Whole blood glucose and β-hydroxybutyrate (β-OHB) levels were measured between 6 and 8 a.m. in tail vein blood at various time points during the study with an Accu-Chek handheld glucometer (Roche Diagnostics, Indianapolis, IN) or a Freestyle Optium Neo ketometer (Abbott Laboratories. Saint-Laurent, QC). Data are expressed in mg/dL.

Assessment of body temperature

Internal body temperature (°C) was measured between 6 and 8 a.m. at various time points during the study with a Thermalert TH-5 thermometer with a flexible rectal probe (Physitemp Instruments, Clifton, NJ).

Animal monitoring in metabolic cages

Indirect calorimetry was performed at the McGill Mouse Metabolic Platform. Animals were individually housed at room temperature (22°C-24°C) in PhenoMaster metabolic cages (TSE Systems, Chesterfield, MO). After 3 days of acclimatization, O_2 consumption, CO_2 production, energy expenditure (heat), respiratory exchange ratio (RER), locomotor activity (beam breaks), and caloric intake were measured. Measurements were made 2 days prior to and for 4 consecutive days after sham surgery or CLP. Average daily metabolic parameters were all normalized to daily body mass. Locomotor activity was simultaneously monitored using infrared sensor frames. Energy expenditure was calculated as $(VO_2*[3.815 + (1.232*RQ)]*4.1868)$. RER was calculated as CO_2 production divided by O_2 consumption.

Autophagic flux quantification

Autophagic flux was monitored in 14–16 weeks old male wild-type C57BL6/J mice subjected to sham or CLP procedures. Briefly, mice received an i.p. injection of the autophagy inhibitor leupeptin (40 mg/kg dissolved in sterile PBS (Sigma-Aldrich # L2884) 20 h post sham or CLP procedures. The sham and CLP control groups received an equivalent volume of sterile PBS. Mice were euthanized 4 hours post leupeptin injection (24h post sham or CLP surgery). Muscles were then rapidly excised and frozen in liquid nitrogen and used for immunoblotting to detect LC3B proteins. Data are shown in Figures S3E–S3F.

In vivo protein synthesis measurements

In vivo protein synthesis in skeletal muscle was measured using the SUnSET technique.[34] Briefly, mice were weighed and injected with intraperitoneally puromycin dissolved in 100 μl of sterile PBS ((0.04 μmol puromycin/ g body mass (Sigma-Aldrich # P8833)). At 30 min post puromycin injection, TA muscles were carefully removed and then frozen in liquid nitrogen and stored (-80°C) for immunoblotting analysis using a mouse IgG2a monoclonal anti-puromycin antibody (clone 12D10, 1:2500; Millipore # MABE343).

Immunoblotting

Portions of frozen muscle samples (≈15-30 mg) were homogenized in an ice-cold lysis buffer (50mM HEPES, 150mM NaCl, 100mM NaF, 5mM EDTA, 0.5% Triton X-100, 0.1 mM DTT, 2 μg/ml leupeptin, 100 μg/ml PMSF, 2 μg/ml aprotinin, and 1 mg/100 ml pepstatin A, pH 7.2) with ceramic beads using Mini-Beadbeater (BioSpec Products, Bartlesville, OK) at 60Hz. Muscle homogenates were kept on ice for 30 min with periodic agitation then centrifuged at 5000 *g* for 15 min at 4°C. Supernatants were collected and pellets were discarded. The protein content in each sample was determined using the Bradford method. Aliquots of crude muscle homogenate were mixed with Laemmli (6X, SDS-sample buffer, reducing, BP-111R) buffer (Boston BioProducts, Ashland, MA) and subsequently denatured for 5 min at 95°C. Equal or equivalent amounts of protein extracts (~20-30 ug per lane) were separated by SDS-PAGE, then transferred onto polyvinylidene difluoride (PVDF) membranes (Bio-Rad Laboratories, Saint-Laurent, QC) using a wet transfer technique. Total protein was detected with Ponceau-S solution (Sigma-Aldrich, #P3504) or with stain-free technology (Bio-Rad). Membranes were blocked in PBS + 1% Tween® 20 + 5% BSA for 1 h at room temperature then incubated overnight with specific primary antibodies at 4°C. Membranes were washed in PBST (3x5 min) then incubated with HRP-conjugated goat anti-rabbit (ab6721) or rabbit anti-mouse (ab6728) secondary antibodies (Abcam, Cambridge, MA) for 1 h at room temperature, before further washing. Immunoreactivity was detected using Pierce™ enhanced

chemiluminescence substrate (Thermo Fisher Scientific, Waltham, MA), a ChemiDoc™ Imaging System, and ImageLab software (Bio-Rad). Optical densities (OD) of protein bands were normalized to a loading control. Immunoblot data are presented relative to sham Atg7$^{f/f}$.

RNA extraction and real-time PCR

Total RNA was extracted from frozen muscle samples using a PureLink™ RNA Mini Kit (Invitrogen Canada, Burlington, ON). Quantification and purity of RNA was assessed using the A260/A280 absorption method. Total RNA (2 μg) was reverse transcribed using a Superscript II® Reverse Transcriptase Kit and random primers (Invitrogen Canada, Burlington, ON). Reactions were incubated at 42°C for 50 min and at 90°C for 5 min. Real-time PCR detection of mRNA expression was performed using a 7500 Sequence Detection System (Applied Biosystems, Foster City, CA). Specific primers (10 μM) were designed to quantify various mRNAs (Table S2). 18S were used as endogenous control transcripts. Each primer (3.5 μl) was combined with reverse-transcriptase reagent (1 μl) and SYBR® Green master mix (25 μl) (Qiagen, Valencia, CA). The thermal profile was as follows: 95°C for 10 min; 40 cycles each of 95°C for 15 s; 57°C for 30 s; and 72°C for 33 s. For each target gene, cycle threshold (C_T) values were obtained. Relative mRNA level quantifications of target genes were determined using the threshold cycle ($\Delta\Delta C_T$) method.

Microarrays

Total RNA was isolated from TA muscle samples (20-25 mg) that were obtained 6 days post-surgery. A total of 21,981 mouse genes were included in the Affymetrix Mouse Clariom S Assay (Affymetrix, Santa Carla, CA) and all steps were performed at the McGill University and Génome Québec Innovation Centre (Montréal, QC). Raw data were pre-processed using Transcriptome Analysis Console (TAC) 4.0.1 software. A limma R software package[76] was used to identify expression level differences between Atg7$^{f/f}$ and Atg7$^{iSkM-KO}$ muscles. Nominal p-values were corrected for multiple testing using the Benjamini-Hochberg method. Genes that showed an FDR of <0.05 were considered statistically significant and differentially expressed (DE). The Canadian Centre for Computational Genomics (C3G) assisted with bioinformatic analyses. Gene Ontology (GO) was used to broadly identify annotation categories of significantly affected molecular function and biological processes. The microarray data are available at the GEO database under the accession number: GSE234838.

QUANTIFICATION AND STATISTICAL ANALYSIS

Unless otherwise indicated, statistical analyses were performed GraphPad Prism 8.0. Data are reported as mean $\pm$ SEM. When only two groups were compared for any given parameter, differences were tested using unpaired bilateral t-tests. Differences between three or more experimental groups were analyzed with one-way analysis of variance (ANOVA) or two-way ANOVA and corrections for multiple comparisons were performed with the two-stage step-up method of Benjamini, Krieger, and Yekutieli (q<0.05 and p<0.05 were considered statistically significant). Comparisons of survival curves were performed using both Mantel-Cox and Gehan-Breslow-Wilcoxon tests. P values of < 0.05 were considered statistically significant. Whenever possible, individual values are displayed in graphs. When individual values could not be displayed, sample sizes are indicated in Figure Legends.